Preprint, accepted for publication in Nature Physics 2018.

Plasmonic Quantum Size Effects in Silver Nanoparticles are Dominated by Interfaces and Local Environments

Alfredo Campos[1], Nicolas Troc[2], Emmanuel Cottancin[2], Michel Pellarin[2], Hans-Christian Weissker[3], Jean Lermé[2], Mathieu Kociak[1] & Matthias Hillenkamp*[2,4]

[1] Laboratoire de Physique des Solides, UMR 8502 CNRS and Université Paris-Sud, Orsay, France

[2] Institut Lumière Matière, Univ. Lyon, Université Claude Bernard Lyon 1, CNRS, UMR5306, F-69622 Villeurbanne, France

[3] Aix Marseille University, CNRS, CINaM UMR 7325, 13288, Marseille, France

[4] Instituto de Física Gleb Wataghin, Universidade Estadual de Campinas, R. Sergio B. de Holanda 777, 13083-859 Campinas-SP, Brazil

Supporting Information

All sections, figures and references in the supporting information are distinguished from the main text by a preceding S.

S1. Supplementary experimental characterization

S1.1 Sample fabrication

An example for the mass selection of silver clusters in the gas phase is shown in Figure S1.1. Cluster ions with less than 20 and more than 38 atoms in this case are efficiently removed from the beam. These spectra were acquired during the thorough calibration of the quadrupole mass spectrometer (QMS, Extrel CMS, USA) transmission with the time-of-flight mass spectrometer (TOF-MS) mounted behind the QMS. Changing the control parameters of the QMS electronics (mass command, ΔM and ΔRes) allows adjusting the transmission window mean and width over a large size range, the low cut-off being limited to ~200 Ag atoms.

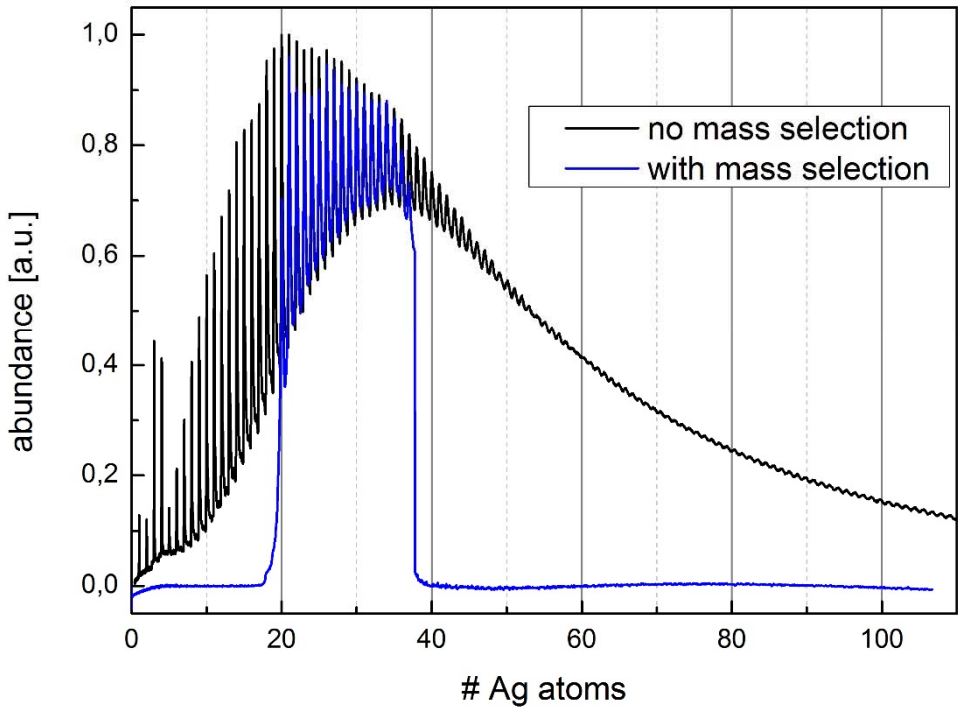

Figure S1.1 TOF-MS spectra with and without mass selection of the QMS.

The absence of coalescence in the samples for optical spectroscopy was verified using conventional TEM of thin films of silica of ~20 nm thickness with embedded silver nanoparticles. Figure S1.2 shows an example image for a sample prepared at two times higher concentration (1 vol.%) than in the sample used for optical experiments. The lower panel shows a typical mass spectrum obtained parallel to the sample fabrication together with the size limits imposed by the QMS (n = 180-400 atoms corresponding to 1.8-2.3 nm diameter) and the diameter histogram from electron microscopy.

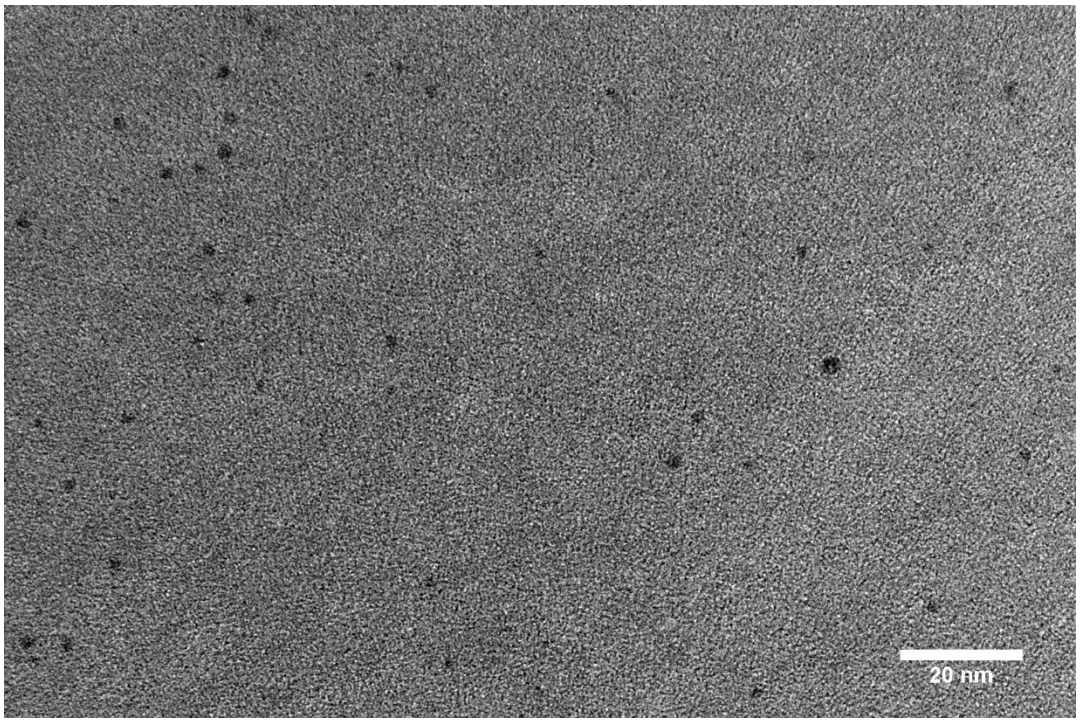

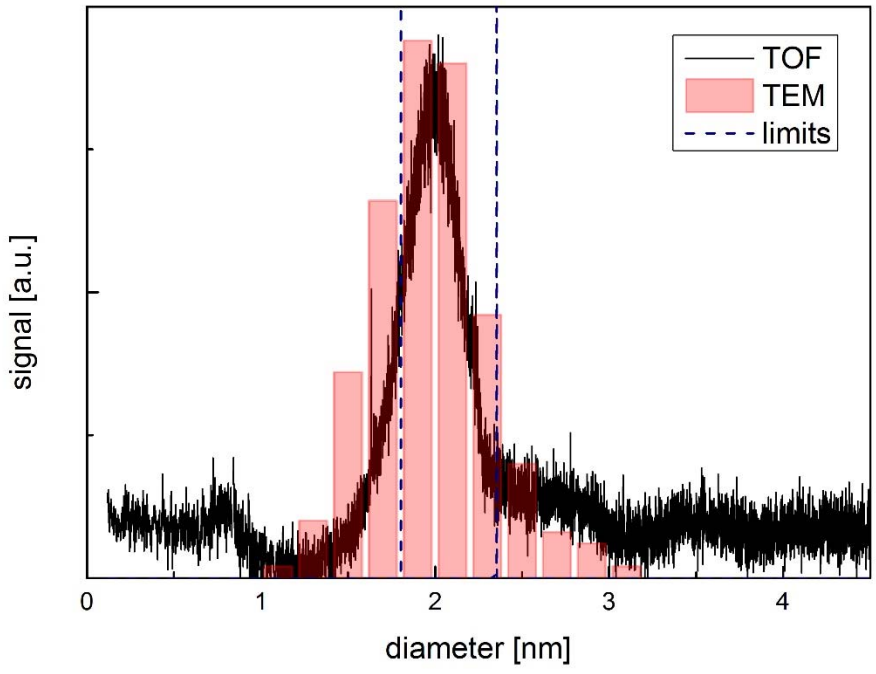

Figure S1.2 top: Example TEM overview image of a thin film sample prepared under identical conditions as the ones used for optical spectroscopy (Fig. 1 in main text). The particles are well separated. Bottom: corresponding Time-of-Flight mass spectrum with the low and high mass cut-offs as defined by the quadrupole mass spectrometer. Also shown is the diameter histogram as derived from TEM.

S1.2 Electron spectroscopy

In this section of the Supporting Information we show more examples for nanoparticle characterization and the effect of electron dose on the particle morphology and on the plasmon resonance.

A particle of ~5nm inside the silica matrix has been observed over a certain time period. Several HAADF images were taken in order to observe the evolution of the particle during the electron irradiation.

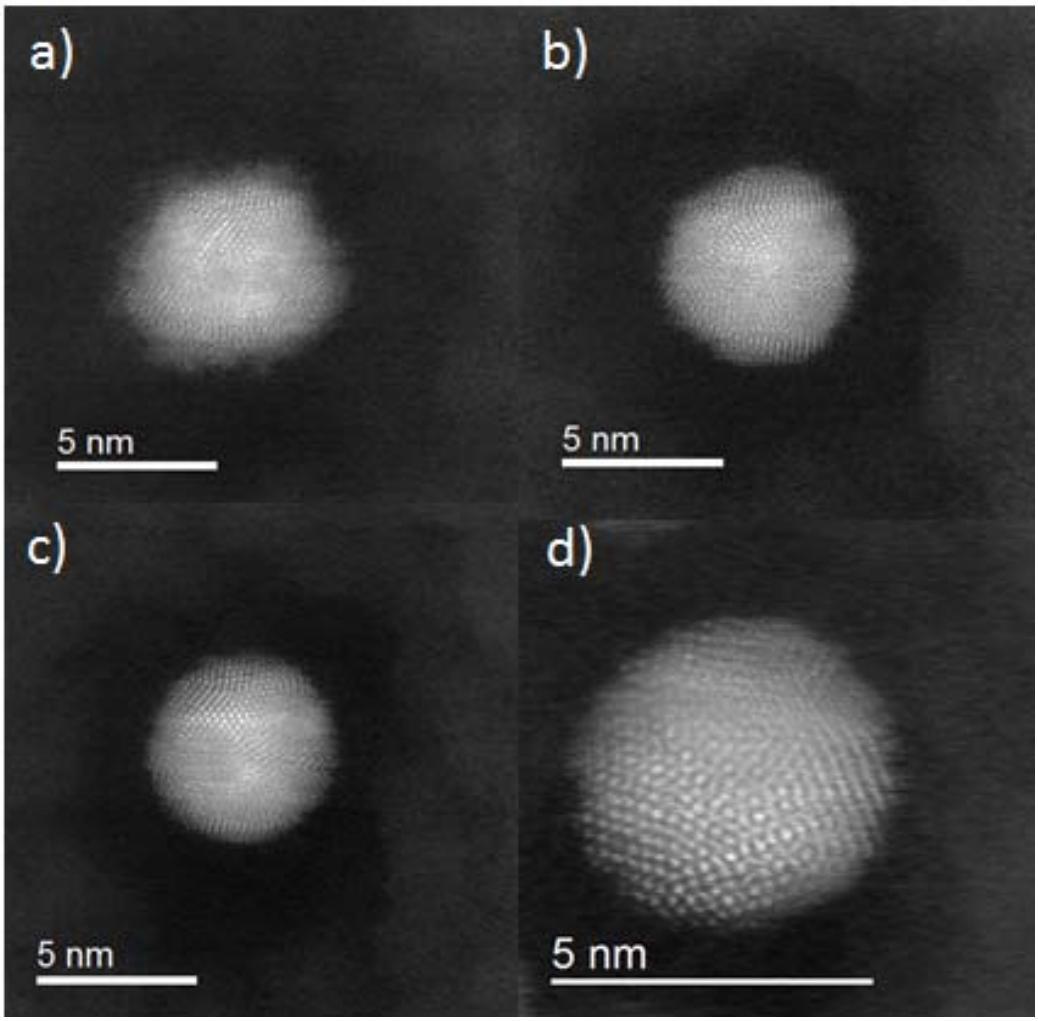

Figure S1.3: Silver particle of ~5 nm diameter at different irradiation doses. From low to high irradiation doses we observe: a) an oxide layer at surface at the beginning of the series. b) The cleaned interface due to the electron irradiation. c) and d) show icosahedral structures at different angles [S1], i.e. the particle rotates under the beam.

In the beginning, most of the particles have an amorphous interface layer which is attributed to oxidation. With increasing accumulated electron dose this shell disappears.

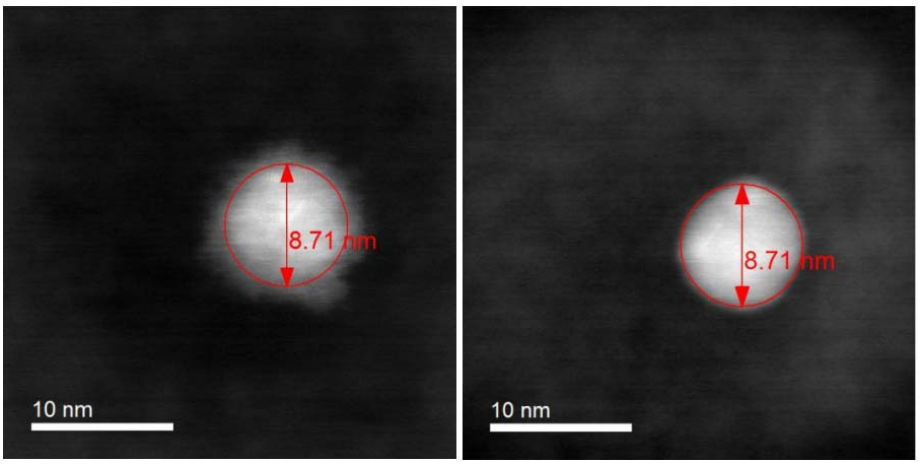

Figure S1.4: Silver particle of 8.7 nm diameter before and after a stack acquisition of 11 spectral images. The acquisition parameters do not allow for atomic-scale imaging. The initially observed amorphous layer around the particle is removed under the electron beam irradiation. The spherical silver particle then no longer changes in size or shape if the electron dose is kept minimal.

In order to evidence the plasmon peak and increase the signal to noise ratio, we sum numerous spectra for beam positions close to the nanoparticle surface, as extracted from a spectrum image and shown in figure S1.5. The signal increases by typically three orders of magnitude, making the signal to noise ratio much larger than 30.

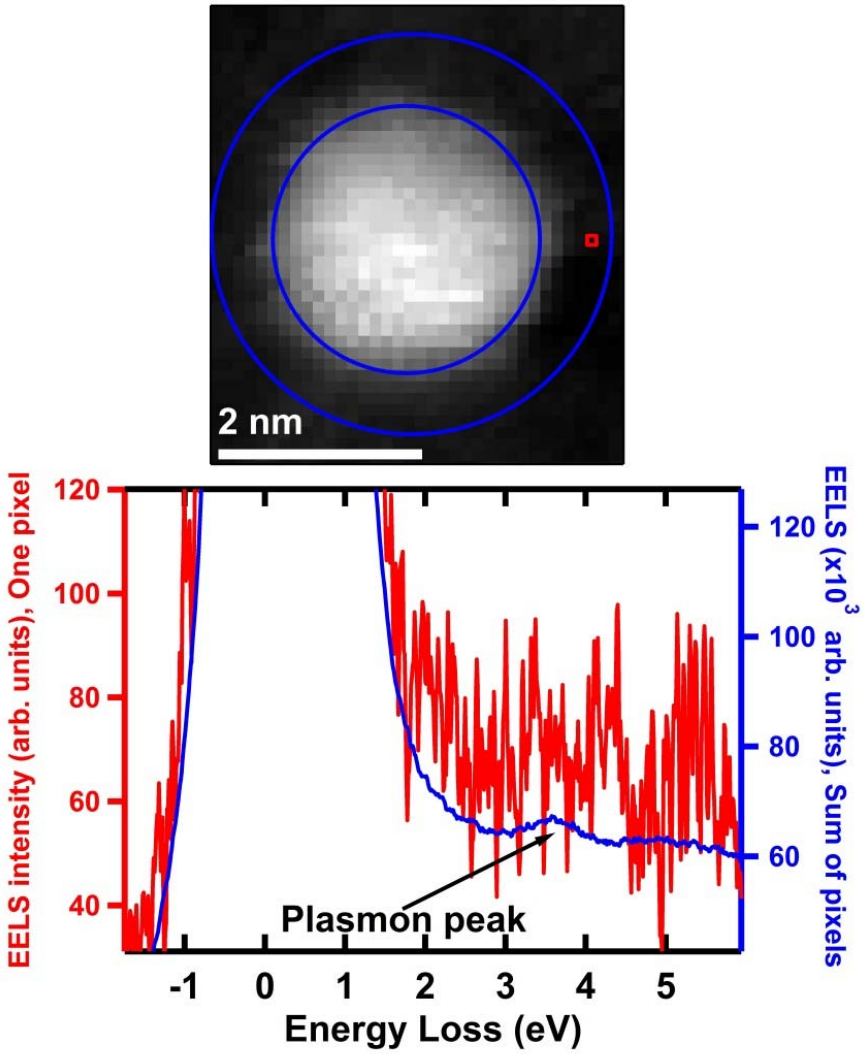

Figure S1.5: Comparison of the spectrum extracted from one pixel (red box and red spectrum) and the spectrum resulting from the sum of the spectra contained in a large number of pixels (region of interest between blue circles; blue spectrum) of a 2.7 nm diameter particle. The plasmon peak is observed only after summing.

One of the difficulties of this experiment is the low plasmon signal of sub-10 nm silver particles, on top of a background due to the zero-loss peak (ZLP). This latter is of comparable intensity – of the order of 10^{-3} of the ZLP maximum, see figure S1.6. A CCD camera with a large dynamic range is needed in order to measure the ZLP (necessary for the energy calibration of the spectrum) and a weak plasmon peak in the same spectrum.

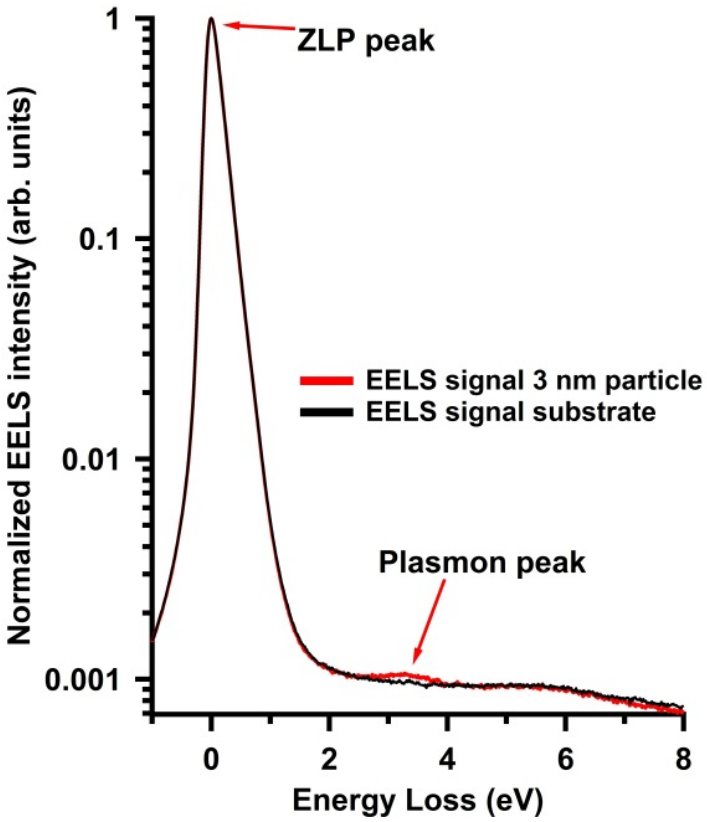

Figure S1.6: EELS signal from the surface of a 3 nm particle, compared to the EELS signal from only the silica matrix on top of the carbon substrate. Note the logarithmic scale for the EELS intensity. In the spectral region of interest the ZLP tail intensity is of the order of 10^{-3} with respect to the ZLP maximum.

As shown in figure S1.7, the surface plasmon energy position was obtained by a least square fitting method. First a ZLP taken on the substrate (covered by silica) is fitted with several Gaussians and the fitting parameters are then used to model the ZLP background on a plasmon signal. The plasmon peak is fitted with a Gaussian peak.

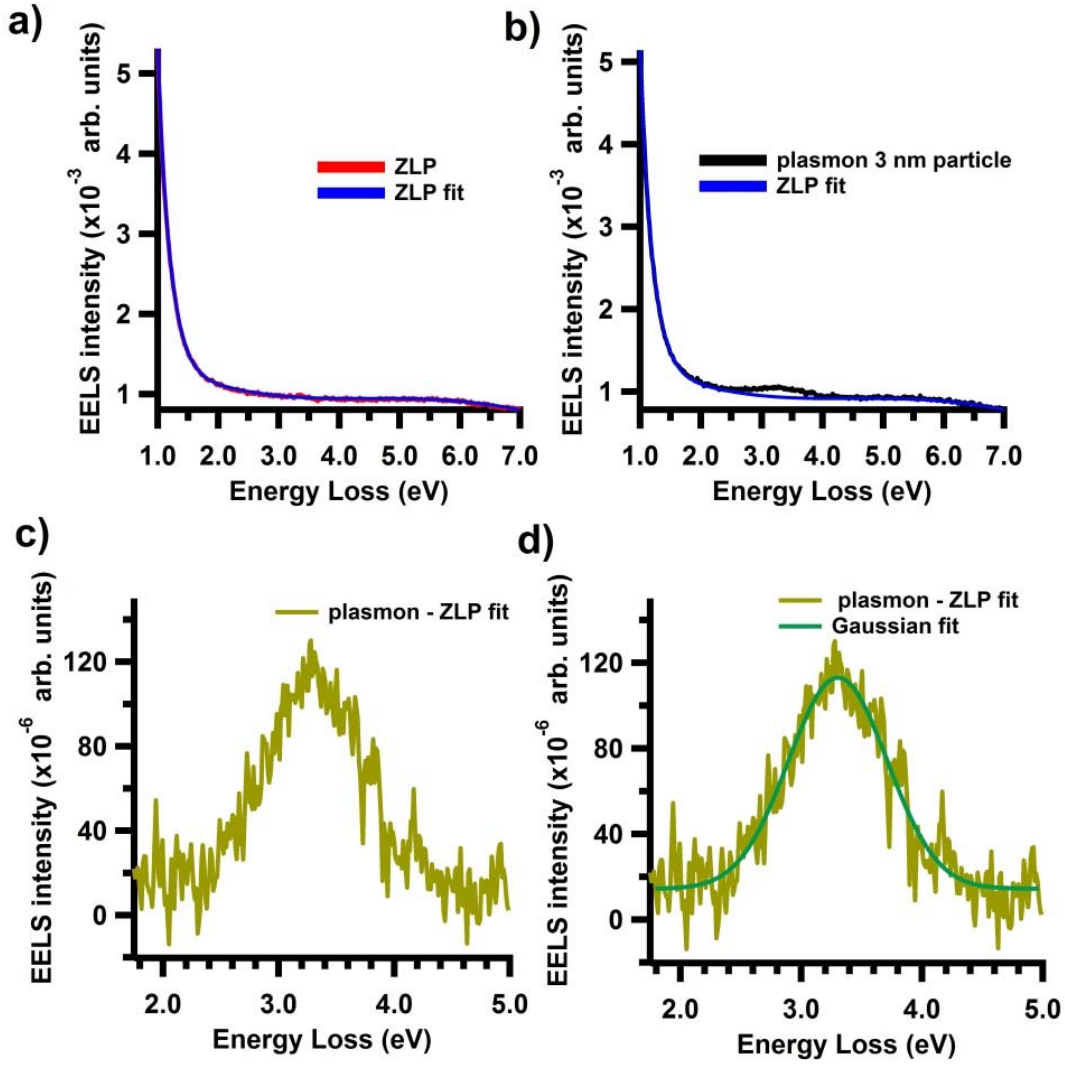

Figure S1.7: Procedure for obtaining the LSPR energy. a) A ZLP taken on the substrate (covered by silica) is fitted with several Gaussians. b) The fitting parameters of the ZLP are used to model the ZLP background of the plasmon signal. c) The modeled ZLP background is then subtracted in order to obtain the LSPR signal. d) A Gaussian fit is used to extract the LSPR energy.

Figure S1.8 presents typical blue shifts of the surface plasmon energy, observed at increasing electron dose for all particle sizes. In most of the cases, there is a large shift at low dose followed by an asymptotic behavior, although saturation is not reached for every nanoparticle. Note that in the smallest particles, the electron dose used was lower in order to avoid particle damage. This is the reason why in some of the smallest particles the LSPR blue shift saturation is not always reached. The steeper rise with electron dose for smaller particles agrees well with the theoretical results as shown in Fig. S2.8, where the same thickness of vacuum layer d_m results in a large shift for small R and a smaller one for bigger R.

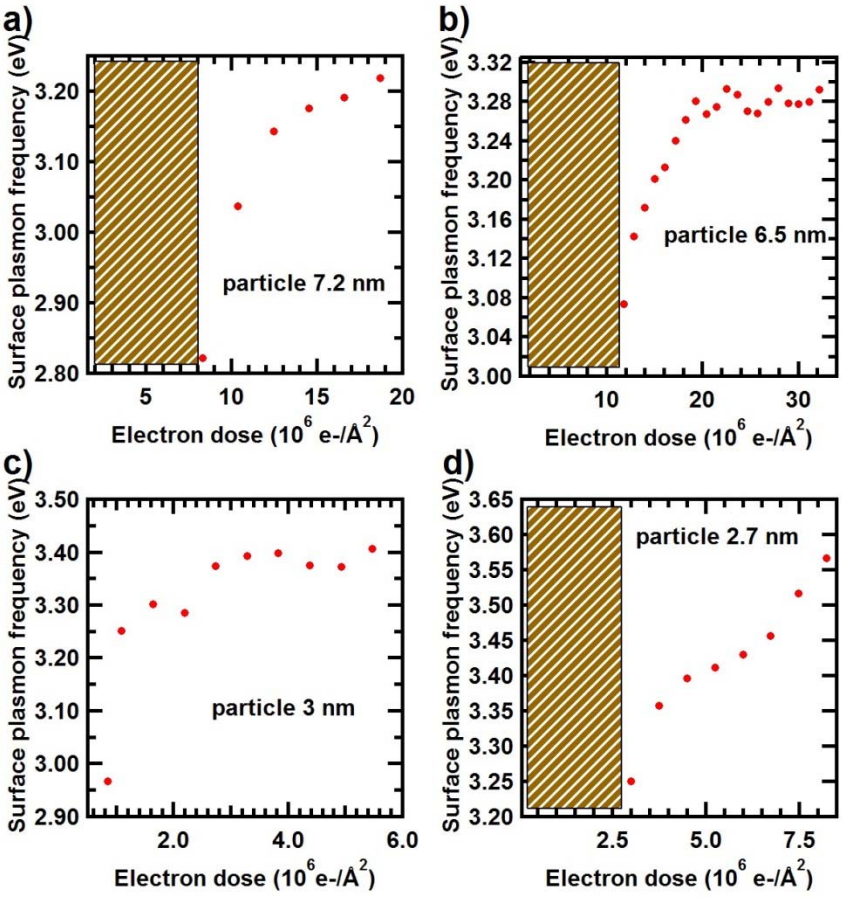

Figure S1.8. Examples of blue shifts of the surface plasmon energy with electron dose for silica-embedded silver particles with diameters of a) 7.2 nm; b) 6.5 nm (same as figure 6a of the main text); c) 3.0 nm; d) 2.7 nm. The shaded area corresponds to doses where no LSPR signal could unambiguously be detected in EEL spectra. At these low doses most particles do not show a LSPR signal due to oxidation.

Note that we have no evidence for changes in matrix stoichiometry. This is reasonable, bearing in mind that light Si and O atoms have, in distinction to heavy Ag, comparable probabilities for being removed from the matrix through knock-on collisions. Furthermore, the LSPR for silver particles of comparable size and embedded in under-stoichiometric silicon oxide matrices has been evidenced at much lower energies than what we observed [S2].

The evolution of the plasmonic response under electron beam irradiation as demonstrated for a large particle in figure 3 of the main text has consistently been observed for all sizes. Another example for a particle of small diameter is shown in figure S1.9.

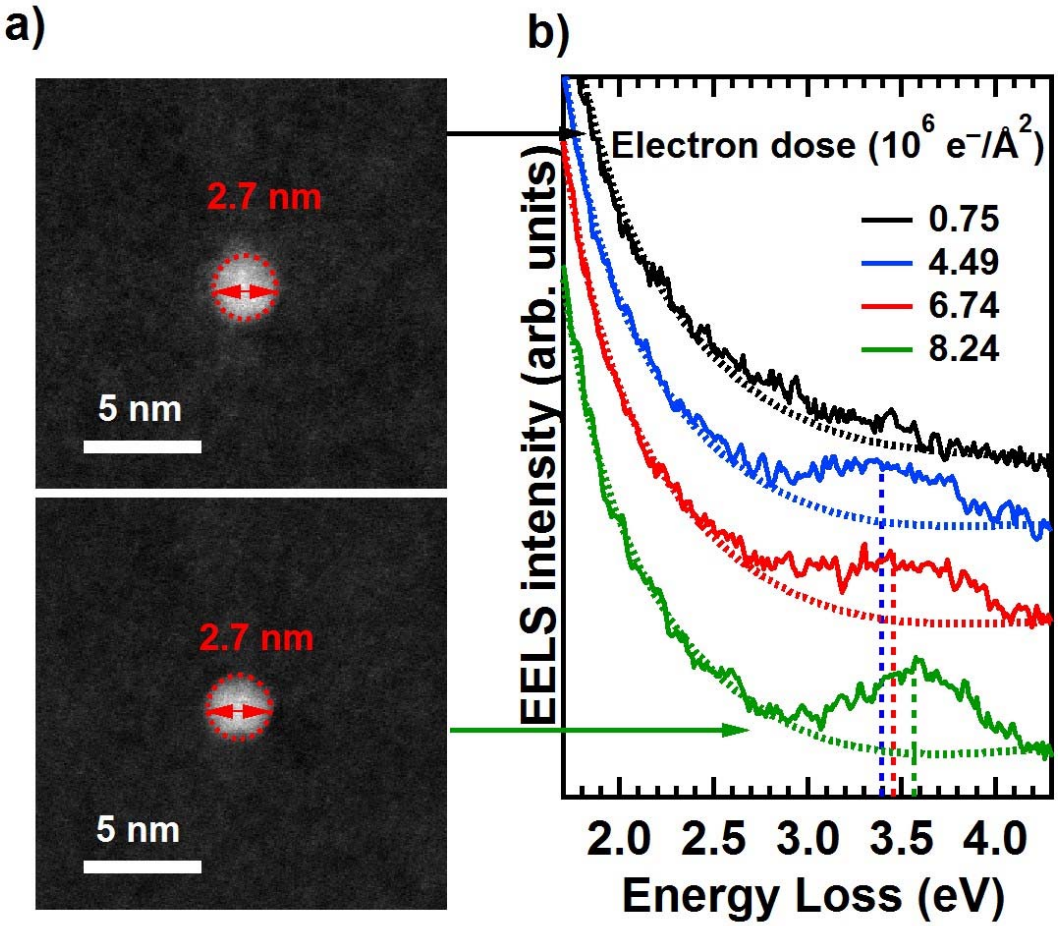

Figure S1.9: Example of electron dose activation of the LSPR in a small particle. a) STEM-HAADF images of a 2.7 nm silver particle diameter embedded in silica at low and high electron dose. The diameter of the particle remains the same. b) Surface plasmon evolution with the electron dose. The surface plasmon is not clear at low electron dose but increases and blue shifts with increasing electron dose. There is also a decrease of line width with increasing electron dose due to a change of environment, consistent with [S2]. The EEL spectra are genuine EELS data with just a ZLP alignment and a sum of pixels around the particle surface. They have been shifted vertically with respect to each other for clarity. The ZLP tails of regions far from the particles are presented in dotted color lines to indicate the zero line for each spectrum.

S2. Supplementary theory

S2.1 Model for electronic spectroscopy of a homogeneous sphere

In order to directly compare LSPR data obtained with optical and electronic spectroscopy, we need to demonstrate the theoretical equivalence between the two methods in our experiments and show the limits of this equivalence. SI units are used throughout this section.

S2.1.1 Non retarded Approximations

In this work, we use the non-retarded approximation.

As noted in [S3], the validity of the non-retarded approximation in EELS relies on several aspects. If one considers the particle itself, the finiteness of the speed of light *c* is important when the propagation time of an electromagnetic wave through the characteristic wavelength (*d*) of the electron cloud oscillation is comparable to its period of oscillation. This condition is obtained when $\omega(d/c) > 1$. In a sphere of radius R, the characteristic wavelength is $d \sim R/\ell$, where ℓ is the mode order. Therefore, retardation becomes significant when $\omega(R/c) > \ell$ [S3]. The particle diameters studied in this article are between 10 and 2 nm, and the resonance energies between 2.7 and 3.7 eV. Thus, $\omega(R/c)$ ranges from 0.019 to 0.068, which is less than 7 % of $\ell = 1$ (dipolar mode) and even smaller for higher orders. This result allows us to neglect retardation effects due to the small size of particles.

Another retardation effect affects the propagation of the electromagnetic field from the electron and back to it, an effect that has to be taken into account in EELS because it enters into the calculation of the work the electron undergoes against the field it induces by polarizing the nanoparticle (see below). The typical distances from the electron beam in the plane of the nanoparticles to any point of the nanoparticle being much less than the typical free space wavelength of the plasmon, this effect can be neglected.

Finally, a last effect concerns the Lorentz contraction. It can be neglected if $\gamma = 1/\sqrt{1-(v/c)^2} \sim 1$. [S3] In the present EELS experiment the electrons are accelerated to 60 kV (~ 0.45 *c*) and the Lorentz gamma factor is $\gamma \sim 1.12$. Although small, the resulting effect is not completely negligible. However, for small spherical metallic particles, the Lorentz contraction factor intervenes only in the probe position dependent function [S4]. Otherwise speaking, it renormalizes the impact factor (here, by ~ 12%), therefore changing the absolute intensity of the simulated EELS spectra. As in the present work we do not consider the absolute intensity of the spectra, this effect is irrelevant for our discussion.

S2.1.2 Energy loss probability in a sphere

This section compiles results from refs [S3-S7].

The energy loss by a fast electron passing near a sample with constant velocity $\mathbf{v}$ along a straight line $\mathbf{r_e}(t)$ can be related to the force exerted by the induced electric field $\mathbf{E_{ind}}$ acting back on the electron [S5]:

$$\Delta E = -e\int_{-\infty}^{\infty} dt\, \mathbf{v}\cdot\mathbf{E_{ind}}\left(\mathbf{r_e}(t),t\right). \tag{2.1.1}$$

The energy loss can be expressed in term of the energy loss probability per unit of frequency $\Gamma(\omega)$:

$$\Delta E = \int_{0}^{\infty} \hbar\omega\, d\omega\, \Gamma(\omega). \tag{2.1.2}$$

Applying the inverse Fourier transform on $\mathbf{E_{ind}}\left(\mathbf{r_e}(t),\omega\right)$ and using the property $\mathbf{E_{ind}}\left(\mathbf{r},\omega\right) = \left[\mathbf{E_{ind}}\left(\mathbf{r},-\omega\right)\right]^*$ we find:

$$\Gamma(\omega) = -\frac{e}{\pi\hbar\omega}\int_{-\infty}^{\infty} dt\, \mathrm{Re}\left\{\mathbf{v}\cdot\mathbf{E_{ind}}\left(\mathbf{r_e},\omega\right)e^{-i\omega t}\right\}, \tag{2.1.3}$$

$$\Gamma(\omega) = \frac{e}{\pi\hbar\omega}\int_{-\infty}^{\infty} dt\, \mathrm{Re}\left\{\mathbf{v}\cdot\nabla V_{ind}\left(\mathbf{r_e},\omega\right)e^{-i\omega t}\right\}. \tag{2.1.4}$$

To determine $V_{ind}\left(\mathbf{r_e},\omega\right)$ we consider a sphere of radius R embedded in a medium and a point electron moving at a constant velocity $\mathbf{v} = -\mathrm{v}\mathbf{e_z}$ along the trajectory $\mathbf{r_e}(t) = \left(x_0, 0, z(t)\right)$, where x_0 is the impact parameter and $z = -\mathrm{v}t$. In order to facilitate calculations, we will work in a spherical reference system with the center placed in the center of the sphere (see figure S2.1). Then the coordinates of the electron will be expressed in the reference system of the sphere. In this spherical system $r_e = \left(x_0^2 + z^2\right)^{1/2}$ and $\cos(\theta_e) = z/r_e = -\mathrm{v}t/r_e$. The potential of the electron at a position $\mathbf{r}$ where $r_e > r$ is [S6, S7]:

$$V_e(\mathbf{r},t) = -\frac{e}{4\pi\varepsilon_0\varepsilon_m\left|\mathbf{r}-\mathbf{r_e}\right|}, \tag{2.1.5}$$

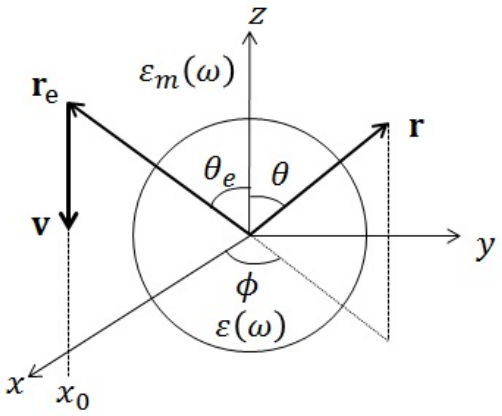

Figure S2.1. Schematics of a sphere embedded in a medium and excited by a fast electron.

which, expressed in a multipole expansion centered on the sphere, writes:

$$V_e(\mathbf{r},t) = -\frac{e}{4\pi\varepsilon_0\varepsilon_m r_e}\sum_{\ell=0}^{\infty}\sum_{m=0}^{\ell} N_{\ell,m}\left(\frac{r}{r_e}\right)^{\ell} P_\ell^m(\cos(\theta))P_\ell^m(\cos(\theta_e))\cos(m\phi), \qquad (2.1.6)$$

where

$$N_{\ell,m} = \frac{(2-\delta_{0m})(\ell-m)!}{(l+m)!}$$

and P_ℓ^m are the associated Legendre polynomials. δ_{0m} is unity if $m=0$ and is zero otherwise.

Applying a Fourier transformation to $V_e(\mathbf{r},t)$ we get:

$$V_e(\mathbf{r},\omega) = -\frac{e}{4\pi\varepsilon_0\varepsilon_m}\sum_{\ell=0}^{\infty}\sum_{m=0}^{\ell} N_{\ell,m} I_{\ell,m} r^{\ell} P_\ell^m(\cos(\theta))\cos(m\phi) \qquad (2.1.7)$$

$$I_{\ell,m}(\omega,x_0) = \int_{-\infty}^{\infty} dt\, r_e^{-(\ell+1)} P_\ell^m(\cos(\theta_e))e^{i\omega t} = \frac{2i^{\ell-m}|\omega/\mathrm{v}|^{\ell} K_m(|\omega x_0/\mathrm{v}|)(\omega/|\omega|)^{\ell-m}}{\mathrm{v}(\ell-m)!},$$

where K_m is the modified Bessel function of second kind.

The induced potentials outside the particle $V_{ind,out}(\mathbf{r},\omega)$ and inside the particle $V_{ind,in}(\mathbf{r},\omega)$ are:

$$V_{ind,out}(\mathbf{r},\omega) = \sum_{\ell=0}^{\infty}\sum_{m=0}^{\ell} a_{\ell,m}(2-\delta_{0m})(R/r)^{\ell+1} P_\ell^m(\cos(\theta))\cos(m\phi), \qquad (2.1.8)$$

$$V_{ind,in}(\mathbf{r},\omega) = \sum_{\ell=0}^{\infty}\sum_{m=0}^{\ell} b_{\ell,m}(2-\delta_{0m})(r/R)^{\ell} P_\ell^m(\cos(\theta))\cos(m\phi). \qquad (2.1.9)$$

Writing $V_e(\mathbf{r},\omega)$ and $V_{ind,out}(\mathbf{r},\omega)$ in the form:

$$V_i(\mathbf{r},\omega)=\sum_{\ell=0}^{\infty}\sum_{m=0}^{\ell} r^{\ell} P_{\ell}^{m}(\cos(\theta))\cos(m\phi)v_{i,\ell,m} \tag{2.1.10}$$

with $i=e$ or ind,out one can define the multipolar polarizabilities as

$$\alpha_{\ell,m}(\omega)=-4\pi\varepsilon_0\varepsilon_m R^{2\ell+1}\frac{v_{ind,out,\ell,m}}{v_{e,\ell,m}}\bigg|_{r=R}. \tag{2.1.11}$$

The multipolar polarizability is the response of the particle to a multipolar excitation of order (ℓ,m).

We assume now that the sphere is made up of a metal of relative permittivity $\varepsilon(\omega)$ embedded in a non-absorbing medium of relative permittivity $\varepsilon_m(\omega)$. We will not take into account non-local effects; therefore, the $\mathbf{q}$ dependency of the dielectric constants is neglected. In the classical limit for the description of the particle response, one can deduce the expression of the multipolar polarizability by using the boundary conditions.

Indeed, the total potential inside or outside the particle, when the electron is outside the particle, is:

$$V_{in/out}(\mathbf{r},\omega)=V_e(\mathbf{r},\omega)+V_{ind,in/out}(\mathbf{r},\omega). \tag{2.1.12}$$

The coefficients $a_{l,m}$ and $b_{l,m}$ of equations 2.1.8 and 2.1.9 can be obtained by the conditions:

$$V_{out}(r=R,\omega)=V_{in}(r=R,\omega), \tag{2.1.13}$$

$$\varepsilon_m\frac{\partial V_{out}(r=R,\omega)}{\partial r}=\varepsilon\frac{\partial V_{in}(r=R,\omega)}{\partial r}. \tag{2.1.14}$$

Finally, the induced potential $V_{ind,out}(\mathbf{r},\omega)$ is:

$$V_{ind,out}(\mathbf{r},\omega)=\frac{e}{4\pi\varepsilon_0\varepsilon_m}\sum_{\ell=1}^{\infty}\sum_{m=0}^{\ell} N_{\ell,m}I_{\ell,m}\frac{R^{2\ell+1}}{r^{\ell+1}}P_{\ell}^{m}(\cos(\theta))\cos(m\phi)\frac{\ell(\varepsilon-\varepsilon_m)}{(\ell\varepsilon+(\ell+1)\varepsilon_m)}. \tag{2.1.15}$$

The term $\ell=0$ does not contribute to the energy loss and is therefore neglected. In the following $V_{ind,out}(\mathbf{r},\omega)$ is just written $V_{ind}(\mathbf{r},\omega)$. The product of $\mathbf{v}$ and $\nabla V_{ind}(\mathbf{r},\omega)$ evaluated at $\mathbf{r}=\mathbf{r_e}$ is:

$$\mathbf{v}\cdot\nabla V_{ind}(r_e,\omega)=\frac{e}{4\pi\varepsilon_0\varepsilon_m}\sum_{\ell=1}^{\infty}\sum_{m=0}^{\ell} N_{\ell,m}I_{\ell,m}\frac{R^{2\ell+1}}{r_e^{\ell+2}}\mathrm{v}(\ell+1-m)P_{\ell+1}^{m}(\cos(\theta_e))\frac{\ell(\varepsilon-\varepsilon_m)}{(\ell\varepsilon+(\ell+1)\varepsilon_m)}. \tag{2.1.16}$$

Introducing equation 2.1.16 in equation 2.1.4 we get:

$$\Gamma(\omega)=\frac{e^2}{4\pi^2\hbar\omega\varepsilon_0\varepsilon_m}\mathrm{Re}\left\{\sum_{\ell=1}^{\infty}\sum_{m=0}^{\ell}\mathrm{v}R^{2\ell+1}N_{\ell,m}I_{\ell,m}I_{\ell+1,m}(\ell+1-m)\left[\frac{\ell(\varepsilon-\varepsilon_m)}{(\ell\varepsilon+(\ell+1)\varepsilon_m)}\right]\right\}, \tag{2.1.17}$$

$$\Gamma(\omega)=\frac{e^2R}{\pi^2\hbar \mathrm{v}^2\varepsilon_0\varepsilon_m}\sum_{\ell=1}^{\infty}\sum_{m=0}^{\ell}M_{\ell,\mathrm{m}}\left[K_m\left(\frac{\omega x_0}{\mathrm{v}}\right)\right]^2\left(\frac{\omega R}{\mathrm{v}}\right)^{2\ell}\mathrm{Im}\left[\frac{\ell(\varepsilon-\varepsilon_m)}{(\ell\varepsilon+(\ell+1)\varepsilon_m)}\right], \qquad (2.1.18)$$

where

$$M_{\ell,m}=\frac{(2-\delta_{0m})}{(\ell-m)!(\ell+m)!}.$$

From equation 2.1.11 we obtain (similar to equation 32 in [S4] except for a prefactor due to a slight difference in the definition of the polarizability):

$$\alpha_{\ell,m}(\omega)=4\pi\varepsilon_0\varepsilon_m R^{2\ell+1}\frac{\ell(\varepsilon-\varepsilon_m)}{\ell\varepsilon+(\ell+1)\varepsilon_m}. \qquad (2.1.19)$$

We note that in the classical limit the multipolar polarizabilities depend only on ℓ and we can simplify the notation to $\alpha_\ell(\omega)$.

Finally we can write:

$$\Gamma(\omega)=\frac{e^2R}{\pi^2\hbar \mathrm{v}^2\varepsilon_0\varepsilon_m}\sum_{\ell=1}^{\infty}\sum_{m=0}^{\ell}M_{\ell,\mathrm{m}}\left[K_m\left(\frac{\omega x_0}{\mathrm{v}}\right)\right]^2\left(\frac{\omega R}{\mathrm{v}}\right)^{2\ell}\mathrm{Im}\left[\frac{\alpha_\ell(\omega)}{4\pi\varepsilon_0\varepsilon_m R^{2\ell+1}}\right], \qquad (2.1.20)$$

$$\Gamma(\omega)=\frac{e^2}{4\pi^3\hbar \mathrm{v}^2(\varepsilon_0\varepsilon_m)^2}\sum_{\ell=1}^{\infty}\sum_{m=0}^{\ell}M_{\ell,\mathrm{m}}\left[K_m\left(\frac{\omega x_0}{\mathrm{v}}\right)\right]^2\left(\frac{\omega}{\mathrm{v}}\right)^{2\ell}\mathrm{Im}[\alpha_\ell(\omega)]. \qquad (2.1.21)$$

These same expressions can be found in [S4, S6] but in a different unit system. Equation (2.1.21) is valid in the local dielectric continuum approximation. However, provided α_ℓ is replaced by $\alpha_{\ell,m}$ and defined as per equation (2.1.11), it can be extended to any other approximation, as discussed later.

S2.1.3 Optical excitation.

As detailed below in section S2.3, the optical absorption cross section is:

$$\sigma_{abs}^{opt}(\omega)=\frac{\omega}{c\varepsilon_0\sqrt{\varepsilon_m}}\mathrm{Im}[\alpha(\omega)], \qquad (2.1.22)$$

where the dipolar polarizability is given by the ratio between the dipolar moment and the incident electric field of a plane wave in the medium.

$$\alpha(\omega)=4\pi\varepsilon_0\varepsilon_m R^3\frac{\varepsilon-\varepsilon_m}{\varepsilon+2\varepsilon_m} \qquad (2.1.23)$$

S2.1.4 Relation between EELS and optical response

From equation 2.1.19:

$$\alpha_{\ell=1}(\omega) = 4\pi\varepsilon_0\varepsilon_m R^3 \frac{\varepsilon-\varepsilon_m}{\varepsilon+2\varepsilon_m} = \alpha(\omega). \tag{2.1.24}$$

The dipolar EELS and optical polarizabilities are therefore equal. The EELS response of a sphere is essentially dipolar when either the impact parameter is large with respect to the sphere diameter and/or the particle diameter is small compared to the free space wavelength of the plasmon. In this case, EELS reads:

$$\Gamma_{\ell=1}(\omega) = \frac{e^2\omega^2}{4\pi^3\hbar \mathrm{v}^4(\varepsilon_0\varepsilon_m)^2}\mathrm{Im}[\alpha(\omega)]\left[\left[K_0\left(\frac{\omega x_0}{\mathrm{v}}\right)\right]^2+\left[K_1\left(\frac{\omega x_0}{\mathrm{v}}\right)\right]^2\right]. \tag{2.1.25}$$

We can obtain a direct relation with the optical absorption cross section:

$$\Gamma_{\ell=1}(\omega) = \frac{ce^2\omega}{4\pi^3\hbar \mathrm{v}^4\varepsilon_0\varepsilon_m{}^{3/2}}\sigma_{abs}^{opt}(\omega)\left[\left[K_0\left(\frac{\omega x_0}{\mathrm{v}}\right)\right]^2+\left[K_1\left(\frac{\omega x_0}{\mathrm{v}}\right)\right]^2\right]. \tag{2.1.26}$$

This equation can in principle also be derived from equation 34 in [S4]. If one only considers the dipolar EELS response of a spherical particle in a non-dispersive material, it is directly proportional to the optical absorption cross section. The energy dependencies of EELS and optical absorption are therefore almost identical close to the resonance (except for an ω prefactor). We also note that the absorption cross section is proportional to the volume of the particle, and if one keeps x_0 constant, both the EELS and absorption cross-sections scale as the volume of the particle.

However, in practical experiments, one does not keep x_0 constant, but rather tries to bring the electron probe as close as possible to the surface of the particle. At small impact parameters and low frequencies (which is the case of small silver nanoparticles embedded in a matrix):

$$[K_1(\omega x_0/\mathrm{v})]^2 >> [K_0(\omega x_0/\mathrm{v})]^2,$$

$$\Gamma(\omega) \approx \frac{ce^2}{4\pi^3\hbar \mathrm{v}^2\varepsilon_0\varepsilon_m{}^{3/2}}\frac{\sigma_{abs}^{opt}(\omega)}{\omega x_0{}^2}. \tag{2.1.27}$$

Therefore, in practical EELS experiments, where we set the impact parameter very close to the surface of the particle $x_0 \approx R$, we get:

$$\Gamma(\omega) \approx \frac{ce^2}{4\pi^3\hbar \mathrm{v}^2\varepsilon_0\varepsilon_m{}^{3/2}}\frac{\sigma_{abs}^{opt}(\omega)}{\omega R^2}. \tag{2.1.28}$$

Since the optical absorption scales as R^3, the EELS probability depends linearly on the radius.

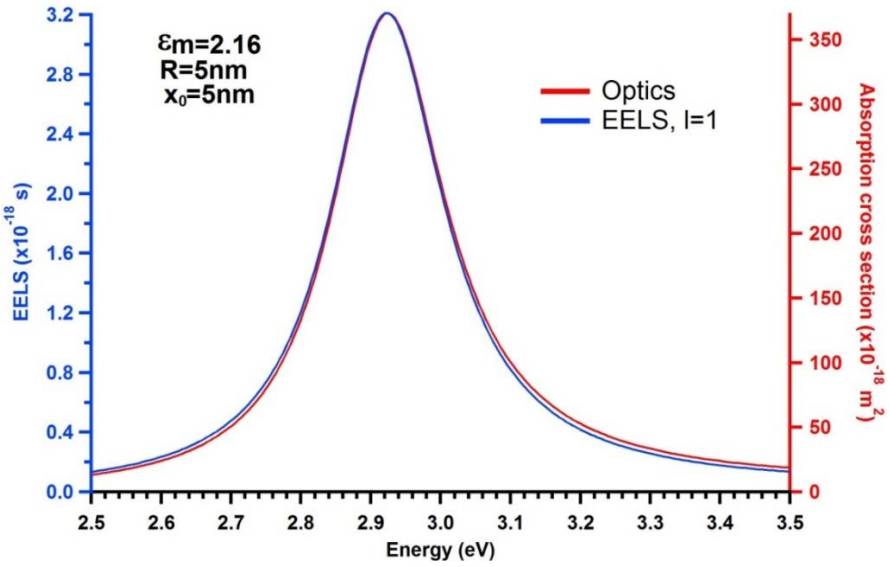

Figure S2.2: Comparison between the Optical absorption cross section from equation 2.1.22 and the EELS dipolar mode $\ell = 1$ from equation 2.1.21. The permittivity of the medium is assumed constant and the permittivity of silver is from the Drude-Lorentz model of Ref. [S8].

S2.1.5 Higher order modes

With equation 2.1.21 we can calculate the EELS probability for higher order modes. After some approximations for the modified Bessel functions of second kind and introducing $\alpha_\ell^{EELS} = \dfrac{\ell(\varepsilon - \varepsilon_m)}{\ell\varepsilon + (\ell+1)\varepsilon_m}$ we obtain:

$$\Gamma_{\ell=1} \approx \frac{e^2 R^3}{\pi^2 \hbar \mathrm{v}^2 \varepsilon_0 {x_0}^2} \mathrm{Im}\left[\alpha_{\ell=1}^{EELS}\right],$$

$$\Gamma_{\ell=2} \approx \frac{e^2 R^5}{3\pi^2 \hbar \mathrm{v}^2 \varepsilon_0 {x_0}^4} \mathrm{Im}\left[\alpha_{\ell=2}^{EELS}\right],$$

$$\Gamma_{\ell=3} \approx \frac{8}{45} \frac{e^2 R^7}{\pi^2 \hbar \mathrm{v}^2 \varepsilon_0 {x_0}^6} \mathrm{Im}\left[\alpha_{\ell=3}^{EELS}\right],$$

$$\frac{\Gamma_{\ell=2}}{\Gamma_{\ell=1}} \approx 0.33 \frac{R^2}{{x_0}^2} \frac{\mathrm{Im}\left[\alpha_{\ell=2}^{EELS}\right]}{\mathrm{Im}\left[\alpha_{\ell=1}^{EELS}\right]},$$

$$\frac{\Gamma_{\ell=3}}{\Gamma_{\ell=1}} \approx 0.17 \frac{R^4}{{x_0}^4} \frac{\mathrm{Im}\left[\alpha_{\ell=3}^{EELS}\right]}{\mathrm{Im}\left[\alpha_{\ell=1}^{EELS}\right]}.$$

Considering the Drude-Lorentz model in [S8] we obtain $\mathrm{Im}\left[\alpha_{\ell=2}^{EELS}\right] / \mathrm{Im}\left[\alpha_{\ell=1}^{EELS}\right] \sim 0.86$ and $\mathrm{Im}\left[\alpha_{\ell=3}^{EELS}\right] / \mathrm{Im}\left[\alpha_{\ell=1}^{EELS}\right] \sim 0.81$ at the resonance conditions. Therefore, at $x_0 \approx R$ (electron beam near the particle surface) we get:

$$\frac{\Gamma_{\ell=2}}{\Gamma_{\ell=1}} \approx 0.28 \text{ and } \frac{\Gamma_{\ell=3}}{\Gamma_{\ell=1}} \approx 0.14$$

The modes $\ell = 2$ and $\ell = 3$ are much less intense than the dipolar mode close to the surface. With the impact parameter increasing the mode $\ell = 2$ decreases as $1/x_0^{\,4}$ and the mode $\ell = 3$ decreases as $1/x_0^{\,6}$. It means that, at large impact parameters, only the dipolar mode is efficiently excited and the electric field felt by the particle is similar to a plane wave like in optical experiments, as already discussed in the literature [S9].

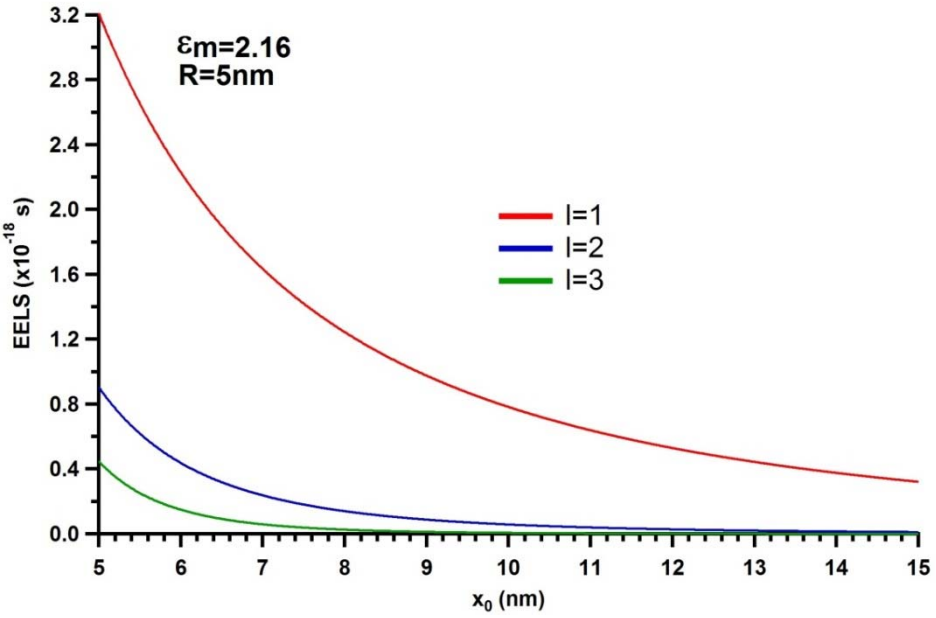

Figure S2.3: EELS signal from equation 2.1.21 for the first 3 modes as a function of the impact parameter. The permittivity of the medium is assumed constant and the permittivity of silver is from the Drude-Lorentz model of Ref. [S8].

As explained in the main text, we suppose that a porous layer around the particle is created by the electron beam irradiation. We have observed experimentally that the EELS signal for impact parameters inside the vacuum layer exhibits a plasmon resonance at the same energy as for larger impact parameters away from the vacuum layer. This means that the contribution to the electron energy loss of the electrons that pass through the vacuum layer can be neglected. The reason is that the force acting back on the electron is essentially perpendicular to the electron velocity when the electron is close to the x-y plane. In consequence the EELS spectrum does not depend critically on the exact value of the impact parameter beyond the particle radius.

S2.2 Link between the dipolar contribution to EELS and the optical absorption

In the preceding Section we have shown that, in the simple case of a matrix-embedded homogeneous sphere, the dipolar electron energy loss probability is proportional to the dipolar optical absorption cross-section. In this Section we will prove that equations (2.1.25) and (2.1.26) in the preceding Section are quite general and actually hold for any spherical systems consisting of an arbitrary number of concentric homogeneous linear media (dielectric or metallic). Moreover, these equations are valid also in the frame of more complex models and/or theoretical approaches, for example when the conduction electrons of the metallic media are described through explicit charge distributions, and when their responses is computed in the frame of a quantum formalism, as the classical/quantum model described hereafter (DFT-TDLDA calculations). We indicate with $R_{\max}$ the overall radius of the system. For a layered system, $R_{\max}$ is the radius of the outermost dielectric interface (including the one related to the layer of reduced matrix refractive index, mimicking the local porosity, if present). In the classical/quantum model used in this work $R_{\max} = \max(R + d_m, R + \delta_{spill})$ where δ_{spill} is the thickness of the electron spillout tail in the ground state (on the order of 2-3 a_0, where a_0 is the Bohr radius). In the following we will define the Fourier transform and its inverse as (to be consistent with the choice made in the previous Section)

$$f(\mathbf{r},t) = \frac{1}{2\pi}\int_{-\infty}^{\infty} d\omega\ f(\mathbf{r},\omega)e^{-i\omega t} \qquad f(\mathbf{r},\omega) = \int_{-\infty}^{\infty} dt\ f(\mathbf{r},t)e^{i\omega t} \tag{2.2.1}$$

The dipolar component of the potential created by the incident electron in the EELS experiment in the radial region $r \le x_0$ (x_0 is the impact parameter), $V_e^{\ell=1}(\mathbf{r},t)$, expresses as

$$V_e^{\ell=1}(\mathbf{r},t) = \frac{1}{2\pi}\int_{-\infty}^{\infty} d\omega \sum_{m=0}^{1} A_{\ell=1,m}(\omega)\, rP_{\ell=1}^{m}(\cos(\theta))\cos(m\phi)e^{-i\omega t}, \tag{2.2.2}$$

with ($I_{\ell=1,m}(\omega)$ and $N_{\ell=1,m}(\omega)$ have been defined in the preceding Section):

$$A_{\ell=1,m}(\omega) = -\frac{e}{4\pi\varepsilon_0\varepsilon_m} N_{\ell=1,m} I_{\ell=1,m}(\omega)\,. \tag{2.2.3}$$

Let us consider the following electric field

$$\mathbf{E}(t) = \frac{1}{2\pi}\int_{-\infty}^{\infty} d\omega \left(E^z(\omega)\mathbf{e}_z + E^x(\omega)\mathbf{e}_x\right)e^{-i\omega t}\,. \tag{2.2.4}$$

The scalar potential corresponding to this field ($\mathbf{E}(t) = -\nabla V_{opt}(\mathbf{r},t)$) writes as

$$V_{opt}(\mathbf{r},t) = \frac{1}{2\pi}\int_{-\infty}^{\infty} d\omega \left(-zE^z(\omega) - xE^x(\omega)\right)e^{-i\omega t}, \tag{2.2.5}$$

$$V_{opt}(\mathbf{r},t)=\frac{1}{2\pi}\int_{-\infty}^{\infty}d\omega\ \sum_{m=0}^{1}\ A_{\ell=1,m}^{opt}(\omega)\ rP_{\ell=1}^{m}(\cos(\theta))\cos(m\phi)e^{-i\omega t}\,, \tag{2.2.6}$$

with $A_{\ell=1,0}^{opt}(\omega)=-E^{z}(\omega)$ and $A_{\ell=1,1}^{opt}(\omega)=-E^{x}(\omega)$. (2.2.7)

The Fourier transforms of $V_{e}^{\ell=1}(\mathbf{r},t)$ and $V_{opt}(\mathbf{r},t)$ are

$$V_{e}^{\ell=1}(\mathbf{r},\omega)=\sum_{m=0}^{1}\ A_{\ell=1,m}(\omega)\ rP_{\ell=1}^{m}(\cos(\theta))\cos(m\phi)\,, \tag{2.2.8}$$

$$V_{opt}(\mathbf{r},\omega)=\sum_{m=0}^{1}\ A_{\ell=1,m}^{opt}(\omega)\ rP_{\ell=1}^{m}(\cos(\theta))\cos(m\phi)\,. \tag{2.2.9}$$

The above equations (2.2.8-9) clearly evidence the close relationship that is expected between EELS and optics, at least for the dipolar term, since the response of any system subject to a given applied potential will not depend on the nature of the source of excitation. Each Fourier component of the induced potential, $V_{ind}(\mathbf{r},\omega)$, inside and outside the system, will be the same in both contexts (EELS and optics), except for a mere multiplicative factor (linear response), that is, $A_{\ell=1,m}(\omega)$ (EELS) or $A_{\ell=1,m}^{opt}(\omega)$ (optics). In particular, outside the system (in the radial region $r>R_{\max}$), each Fourier component of the induced potential satisfies the homogeneous Laplace equation $\Delta V_{ind}(\mathbf{r},\omega)=0$, whatever the complexity of the system and the theoretical approach (note that in a classical dielectric description $\Delta V_{ind}(\mathbf{r},\omega)=0$ holds also in the radial region $r<R_{\max}$). Outside the system, each Fourier component $V_{ind}(\mathbf{r},\omega)$ expresses thus as

$$V_{ind}^{\ell=1,m}(\mathbf{r},\omega)=\sum_{m=0}^{1}\ \frac{D_{\ell=1,m}(\omega)}{r^{2}}P_{\ell=1}^{m}(\cos(\theta))\cos(m\phi)\,, \tag{2.2.10}$$

with $D_{\ell=1,m}(\omega)=D'_{\ell=1,m}(\omega)A_{\ell=1,m}(\omega)$ (EELS) or $D_{\ell=1,m}(\omega)=D'_{\ell=1,m}(\omega)A_{\ell=1,m}^{opt}(\omega)$ (optics),

where the coefficient $D'_{\ell=1,m}(\omega)$ depends only on the system, but not on the physical context.

In the context of optics equation (2.2.10) thus writes as

$$V_{ind}^{\ell=1,m}(\mathbf{r},\omega)=\sum_{m=0}^{1}\ \frac{D'_{\ell=1,m}(\omega)A_{\ell=1,m}^{opt}(\omega)}{r^{2}}P_{\ell=1}^{m}(\cos(\theta))\cos(m\phi)\,. \tag{2.2.11}$$

The dipolar optical polarizability $\alpha_{\ell=1}(\omega)$ (*m*-independent because of the spherical symmetry of the system) is defined through the relationship linking the Fourier *m*-components of the induced dipole $\mathbf{p}(t)$ and applied electric field $\mathbf{E}(t)$:

$$p_{\ell=1,m}(\omega)=\alpha_{\ell=1}(\omega)(-A_{\ell=1,m}^{opt}(\omega)) \tag{2.2.12}$$

(the *z*- and *x*-components of the Fourier component $\mathbf{p}(\omega)$ correspond to *m* = 0 and *m* = 1, respectively).

From the well-known expression of the dipolar potential created by a dipole **p**, namely $V(\mathbf{r}) = (1/4\pi\varepsilon_0\varepsilon_m)\mathbf{p}\cdot\mathbf{r}/r^3$, the Fourier component of the induced potential can be expressed as

$$V_{ind}(\mathbf{r},\omega) = \frac{1}{4\pi\varepsilon_0\varepsilon_m}\sum_{m=0}^{1}\frac{\alpha_{\ell=1}(\omega)(-A^{opt}_{\ell=1,m}(\omega))}{r^2}P^m_{\ell=1}(\cos(\theta))\cos(m\phi)\,. \qquad (2.2.13)$$

From equations (2.2.11) and (2.2.13) one obtains the general equation linking $D'_{\ell=1,m}(\omega)$ and $\alpha_{\ell=1}(\omega)$

$$D'_{\ell=1,m}(\omega) = -\frac{\alpha_{\ell=1}(\omega)}{4\pi\varepsilon_0\varepsilon_m}\,. \qquad (2.2.14)$$

In the case of a homogeneous sphere we have $D'_{\ell=1,m}(\omega) = R^3\frac{\varepsilon_m-\varepsilon(\omega)}{\varepsilon(\omega)+2\varepsilon_m}$. (2.2.15)

Let us recall that the EELS theory reported in the preceding section requires: (i) the suitability of the $V_e(\mathbf{r},t)$ expression, given in equation (2.1.6), which is valid only in the radial zone $r_e \geq r$, and (ii) the condition $x_0 > R_{\max}$ ($R_{\max} = R$ for a homogeneous sphere). As a consequence, the force acting back on the electron depends only on the induced potential in the radial zone $r > R_{\max}$ [equation (2.2.11) with $A^{opt}_{\ell=1,m}(\omega)$ replaced by $A_{\ell=1,m}(\omega)$], and thus only the coefficient $D'_{\ell=1,m}(\omega)$ is necessarily involved in the expression for $\Gamma(\omega)$. This allows the dipolar contribution to the energy loss probability $\Gamma(\omega)$ (equation (2.1.18)) to be expressed as

$$\Gamma_{\ell=1}(\omega) = \frac{e^2}{\pi^2\hbar\,\mathrm{v}^2\varepsilon_0\varepsilon_m}\sum_{m=0}^{1} M_{\ell=1,m}(K_m(\frac{\omega\,x_0}{\mathrm{v}}))^2\frac{\omega^2}{\mathrm{v}^2}\ \mathrm{Im}(-D'_{\ell=1,m}(\omega))\,. \qquad (2.2.16)$$

Using the general relationship equation (2.2.14), one finally obtains ($M_{\ell=1,m}=1$)

$$\Gamma_{\ell=1}(\omega) = \frac{e^2\omega^2}{4\pi^3\hbar\,\mathrm{v}^4\varepsilon_0^2\varepsilon_m^2}\sum_{m=0}^{1}(K_m(\frac{\omega\,x_0}{\mathrm{v}}))^2\ \mathrm{Im}(\alpha_{\ell=1}(\omega))\,. \qquad (2.2.17)$$

Equations (2.1.25) and (2.1.26) in the preceding section are thus quite general, suitable for any spherically symmetric system, provided that $x_0 > R_{\max}$.

S2.3 Theoretical model for optical spectroscopy

In order to interpret the experimental findings, absorption spectra of free and silica-embedded silver particles have been computed in the framework of a mixed classical/quantal jellium-type model of concentric nested dielectric background media and over a large size range (up to 5000 atoms in the present work, corresponding to a diameter of 5.5 nm). The limits of applicability of the method and its relation with other approaches are discussed at the end of this section. The main focus is on the interpretation of the size evolution of the spectral location of the LSPR band (energy $\hbar\omega_M$), which, in the studied size range, reflects to a large extent quantum finite-size effects. In particular, these investigations aim at explaining the different size dependencies that are observed in the absorption spectroscopy and EELS experiments. This model was successfully applied in previous works to alumina-embedded noble metal nanoclusters, allowing the observed size evolutions for Ag, Au and Cu to be rationalized in a common theoretical framework [S10-S12]. In fact, for matrix-embedded noble metal clusters, the size evolution of the LSPR frequency was found to be determined by the competition between opposite trends, namely the red- and blue-shifts induced by, respectively, (i) the spill-out effect, and (ii) the surface layer of ineffective ion-core polarizability, as well as by the local porosity at the metal/matrix interface. Indeed, this subtle competition explains probably the success of classical Mie theory in the small-size range (quasistatic limit) for these species, especially for silver, as compared to free small alkali clusters, for which the spillout-induced quantum size effect is not compensated.

The calculations are based on (i) the time-dependent local-density-approximation formalism (TDLDA) for computing the optical response, and, (ii) the density functional theory (DFT) for computing the ground-state. As compared to pioneering formalisms, suitable for free alkali jellium spheres [S13], the present model includes phenomenologically (but self-consistently) the absorption/screening properties of the ionic core background (effects related to the bulk interband-transitions contribution) and the screening properties of the surrounding transparent matrix [S14, S15]. In particular, the model describes self-consistently the mutual interplay between the optical excitations and induced fields in the various media. As compared to simple free-electron metals, such as alkalis, the optical properties of noble metal clusters are more complex because interband transitions occur in the visible-near UV spectral range. These transitions correspond to electronic excitations from fully-occupied d-valence electron bands, located close below the Fermi energy E_F (4d bands for Ag), to unoccupied s-p levels above E_F, and are responsible for the large signal increase in the absorption spectra above 4 eV (see e.g. Fig. 1 in the main text). The interband threshold $\hbar\Omega_{ib}$ for silver is of the order of 3.9 eV ($\lambda \approx 320$ nm) and consequently the d-bands act essentially through dynamical screening effects in the LSPR spectral range ($\hbar\Omega_{ib} > \hbar\omega_M$) without inducing concomitant LSPR broadening, contrary to gold and copper ($\hbar\Omega_{ib} \approx 2$ eV).This screening, induced by the ionic-core polarization, reduces the strength of the bare Coulomb interaction, in particular the restoring force by the positively-charged jellium, and leads to a strong spectral shift towards lower energies of the LSPR frequency (for large free silver clusters, the collective oscillation of the conduction s-p electron gas would occur at $\omega_M \approx 5.2$ eV in the absence of d-band-induced screening).

Regarding the metal particle, the conduction electrons, corresponding to the bulk s-p band, responsible for the collective surface plasmon excitation and underlying most of the (quantum) finite-size effects, are quantum mechanically treated, whereas the ionic background is phenomenologically described by both: (i) a step-walled homogeneous spherical positively-charged distribution (*jellium*) of radius $R = r_s N^{1/3}$ (r_s is the Wigner-Seitz (WS) radius per conduction electron in the bulk and *N* the number of electrons), and, (ii) a homogeneous polarizable/absorbing dielectric medium [frequency-dependent relative complex dielectric function $\varepsilon_{ib}(\omega)$ (dimensionless input data of the model), corresponding to the interband transitions, assumed to be bulk-like] extending up to $R_1 = R-d$, where *d* is the skin thickness of ineffective ion polarizability (cf. Fig. 5 in the main text).

This last ingredient needed, which is of main importance for explaining the finite-size effects in noble metal clusters, as compared to alkali elements, deserves to be commented on. This skin of vanishing polarizability was introduced by Liebsch [S16] in the context of electron energy loss at metal surfaces, and applied early to rare-gas matrix-embedded Ag_N-clusters within a classical approach involving concentric nested dielectric media [S17]. This surface property, subsequently discussed by several authors [S10, S18, S19], is thought to be related to both the spatial localization of the d-electron wavefunctions relative to the Wigner-Seitz radius [S18] and the change of the effective polarizability of the ionic-cores depending on the embedding medium or local environment [S19]. Strictly speaking, the thickness *d* has to be considered as a free phenomenological parameter. In view of the approximation consisting in replacing the discrete ionic structure by homogeneous step-walled jellium and dielectric medium, a rigorous prescription for setting its value cannot be defined. In this work the value has been set in order to reproduce the experimental finite-size effects observed in free Ag_N^+ clusters [S10, S20]. This procedure leads to the value $d \approx 3.5\ a_0$ (a_0 is the Bohr radius), on the order of the WS radius per conduction electron in bulk silver. This value was systematically used in our previous works [S10-S12].

The relative complex dielectric function $\varepsilon_{ib}(\omega)$ has been carefully extracted from the experimental complex dielectric function $(\varepsilon_{\exp}(\omega) = \varepsilon_{ib}(\omega) + \varepsilon_D(\omega) - 1)$ of bulk silver [S21] by a Kramers-Kronig analysis after subtracting the conduction-electron contribution $\varepsilon_D(\omega)$, parametrized by a Drude-Sommerfeld formula (see ref. [S11] for the details of the procedure). Briefly, the imaginary component $\mathrm{Im}(\varepsilon_{ib}(\omega))$ is first extracted from the imaginary component of the experimental bulk dielectric function, which exhibits a steep rising edge at the interband threshold. The real component is then calculated using to the Kramers-Kronig relation linking both components. For this extraction the interband threshold $\hbar\Omega_{ib}$ = 3.85 eV has been assumed (extrapolation to zero of the low-energy rising edge of $\mathrm{Im}(\varepsilon_{\exp}(\omega))$). The following bulk parameters for r_s and *m* (effective optical electron mass), entering the conduction electron contribution $\varepsilon_D(\omega) = 1 - \omega_P^2/(\omega(\omega + i\gamma))$, have been used [$\omega_P = (3q^2/4\pi\varepsilon_0 r_s^3 m)^{1/2}$ is the bulk plasma frequency]: r_s = 3.02 bohr [S22] and $m = m_e$ (free electron mass) [S23]. The damping factors γ have been estimated in fitting $\mathrm{Im}(\varepsilon_{\exp}(\omega))$ with $\mathrm{Im}(\varepsilon_D(\omega))$ in

the spectral range below $\hbar\Omega_{ib}$. It should be emphasized that the interband contribution $\varepsilon_{ib}(\omega)$ obtained through this procedure depends only very slightly on the selected Drude-parameters, because above the interband threshold $\hbar\Omega_{ib}$, the largest part of $\mathrm{Im}(\varepsilon_{\exp}(\omega))$ is exhausted by $\mathrm{Im}(\varepsilon_{ib}(\omega))$. Therefore, the accuracy depends essentially on the reliability of the experimental data.

As far as the dielectric function $\varepsilon_m(\omega)$ of the transparent embedding matrix is concerned, all calculations have been carried out by using the tabulated bulk-silica data [S21]. In the visible spectral range $\varepsilon_m(\omega)$ varies only slightly and is on the order of 2.16 around 3 eV. Previous works on composite films involving noble metal clusters embedded in alumina have shown that the matrix porosity, especially in the close vicinity of the metal particles, has a strong impact on the optical properties [S10, S12]. An additional and noticeable blue-shift of the LSPR frequency, relative to the prediction obtained by using the bulk refractive index of alumina, was clearly evidenced. More specifically, the *local* porosity at the metal/matrix interface (surface roughness, contact defects, different chemical nature of the constituents, etc…), that results in a lowering of the local effective matrix polarizability, has a very strong influence. As stated in the experimental section, the time-evolution of the single-particle EELS spectra as well as the STEM-HAADF images suggest that, due to damage induced by the electron beam, a continuous removal of matter occurs during the irradiation, creating a porous silica layer of reduced refractive index around the particle. As in previous works, a vacuum shell of thickness d_m is introduced in the model in order to mimic phenomenologically the spherically-averaged local porosity. Obviously, for ensuring a given LSPR blue-shift, a larger d_m-value would be necessary if a larger relative refractive index (> 1) was assumed for characterizing this very porous silica shell.

The mixed classical/quantal model thus involves three nested spherical interfaces (see Fig. 5 in the main text), located at $r = R_1 = R - d$, $r = R$ and $r = R_2 = R + d_m$, but two background dielectric interfaces separating three homogeneous background media ($\varepsilon_b(\omega) = \varepsilon_{ib}(\omega)$ for $r < R_1$, $\varepsilon_b(\omega) = 1$ for $R_1 < r < R_2$ and $\varepsilon_b(\omega) = \varepsilon_m(\omega)$ for $r > R_2$).

The computations have been carried out using a home-written computer code based on the TDLDA formalism including phenomenologically, but self-consistently, the absorption and polarization properties of the underlying backgrounds (core d-electrons and surrounding matrix) through macroscopic dielectric functions [S14, S15]. A brief description of the mixed classical/quantal model is provided hereafter (SI units are used; convenient units, namely eV and nm, are, however, also used for displaying the results).

The first step consists in determining the ground state of the system, namely in solving iteratively the Kohn-Sham (KS) equations

$$\left\{-\frac{\hbar^2}{2m}\nabla^2 + V_{eff}(\rho,\mathbf{r})\right\}\varphi_i(\mathbf{r}) = \varepsilon_i\varphi_i(\mathbf{r})\,. \qquad (2.3.1)$$

The single-electron effective KS potential $V_{eff}(\rho,\mathbf{r})$ is a functional of the electron density $\rho(\mathbf{r})$ and includes the interactions with the homogeneous charge distribution $\rho_+(\mathbf{r})$ of the jellium sphere ($\rho_+(\mathbf{r}) = q\rho_{0+}H(R-r)$ where $\rho_{0+} = 3/(4\pi r_s^3)$, $H(x)$ the Heaviside step-function and q the elementary charge) and with the conduction electron charge density $-q\rho(\mathbf{r})$ (the so-called classical Coulomb term), as well as the exchange-correlation contribution

$$V_{eff}(\rho,\mathbf{r}) = V_{e-jel}(\mathbf{r}) + V_{e-e}(\rho,\mathbf{r}) + V_{xc}(\rho(\mathbf{r})), \tag{2.3.2}$$

with

$$V_{e-e}(\rho,\mathbf{r}) + V_{e-jel}(\mathbf{r}) = \frac{q^2}{4\pi\varepsilon_0}\int V_c(\mathbf{r},\mathbf{r}')\,(\rho(\mathbf{r}') - \rho_+(\mathbf{r}'))d^3r' \tag{2.3.3}$$

and

$$V_{xc}(\rho(\mathbf{r})) = \frac{\delta E_{xc}(\rho)}{\delta\rho(\mathbf{r})}. \tag{2.3.4}$$

In eq (2.3.3) $(q^2/(4\pi\varepsilon_0))V_c(\mathbf{r},\mathbf{r}')$ is the effective Coulomb interaction between two free elementary charges, located at **r** and **r'**, in the presence of the polarizable background-dielectric media. $V_c(\mathbf{r},\mathbf{r}')$ depends on the parameter set $\{R_1, R_2, \varepsilon_{ib}, \varepsilon_m\}$ ($V_c(\mathbf{r},\mathbf{r}',\omega) = 1/|\mathbf{r}-\mathbf{r}'|$ in the absence of underlying dielectric media). Different $V_c(\mathbf{r},\mathbf{r}')$-expressions prevail, depending on the values of *r* and *r'* relative to the dielectric interface radii R_i. The analytical formulas for one and two concentric dielectric interfaces can be found in ref [S11]. Note that, in this first step (determination of the ground-state), the static values $\varepsilon_b(\omega = 0)$ are involved.

As in our previous studies, in particular refs. [S14, S15], the local Gunnarsson-Lundqvist exchange-correlation energy functional $E_{xc}(\rho)$ [S24], of widespread use in the cluster physics literature [S13, S25], has been used throughout the present work. It is worthwhile noting that this functional was also used by Toscano *et al*. in the frame of a sophisticated hydrodynamic model [S26], allowing the self-consistent TDLDA results reported hereafter to be compared with those of the hydrodynamic model.

Typical results are shown in Figure S2.4. This Figure displays the normalized ground-state electron density $\rho_{gs}(r)/\rho_{0+}$ and the effective KS potential $V_{eff}(\rho_{gs},r)$ for the parameter set [*N* = 832 (*R* ≈ 1.5 nm), *d* = 3.5 a_0 and d_m = 2 a_0]. Clearly visible are the diffuse surface profiles of the electron density and of the confining finite-depth potential. These quantum finite-size features contrast dramatically with those assumed, often implicitly, within oversimplified quantum/classical models (mostly, an infinite potential barrier model, and/or an electron density matching perfectly the homogeneous step-walled jellium, are used), explaining why these latter may lead to incorrect size trends [S27, S28]. It should be emphasized that these unphysical models may, fortuitously, reproduce the experimental results,

because the net size trend observed in a real experiment often results from the competition between opposite size trends, as stated previously. Nonetheless no physical insight is gained from these unrealistic models. These points will be illustrated in the following.

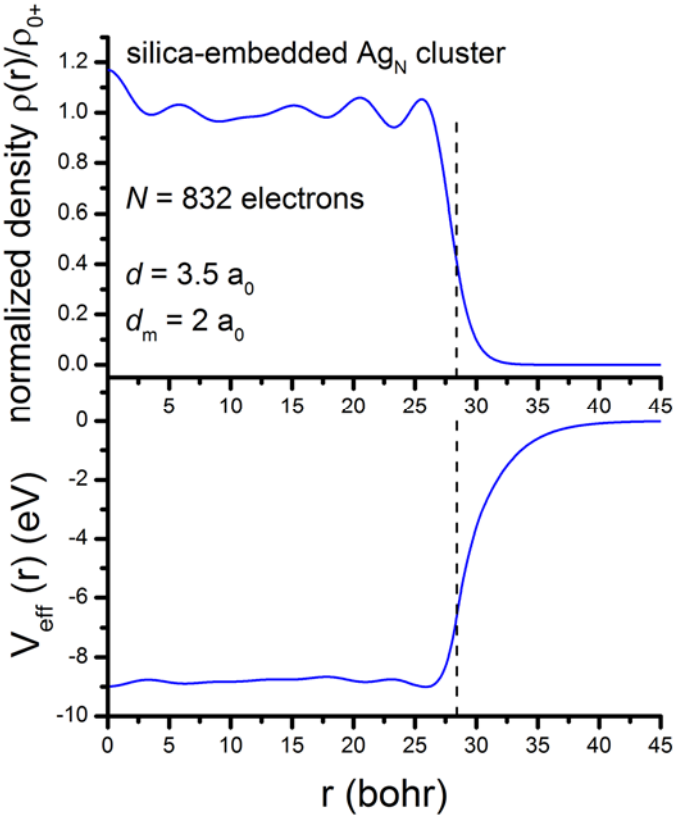

Figure S2.4: Results of the ground-state calculation for silica-embedded Ag_{832} cluster (size N = 832; $R \approx 28.4\ a_0$), with d = 3.5 a_0 and d_m = 2 a_0, computed within the Kohn-Sham DFT formalism. Upper panel: Self-consistent ground-state electron density normalized to the jellium density $\rho_{0+} = 3/(4\pi r_s^3)$. Lower panel: Kohn-Sham confining potential.

The second step consists in computing the optical response within the TDLDA formalism. In response to an applied monochromatic field of frequency ω, $\mathbf{E}_0(t) = E_0 e^{-i\omega t}\mathbf{e}_z$, the "matrix-embedded particle" is polarized, giving rise to a total dipole $\mathbf{p}(t) = \alpha(\omega)\mathbf{E}_0(t)$, and -in particular- a time-varying electronic density $\delta\rho(\mathbf{r},\omega)e^{-i\omega t}$ is induced inside the metal sphere (conduction electron density). The electron density is thus $\rho(\mathbf{r},t) = \rho_{gs}(\mathbf{r}) + \delta\rho(\mathbf{r},\omega)e^{-i\omega t}$. The above terminology "matrix-embedded particle" is intentionally used to keep in mind that the metal particle (the conduction electrons and the polarizable ionic cores) *and* the matrix underlie the induced dipolar field. To this applied external field corresponds, in the non-retarded quasistatic limit, the electron potential energy $V_{ext}^{bare}(\mathbf{r},\omega)e^{-i\omega t}$, with $V_{ext}^{bare}(\mathbf{r},\omega) = qzE_0$ (usually referred to as the "external, or applied, potential energy" in the standard

TDLDA formalism). The absorption cross-section $\sigma_{abs}^{opt}(\omega)$ is related to the imaginary component of the overall complex dynamical polarizability $\alpha(\omega)$ via the equation

$$\sigma_{abs}^{opt}(\omega) = \frac{\omega}{c\varepsilon_0\sqrt{\varepsilon_m(\omega)}}\mathrm{Im}[\alpha(\omega)]\,. \tag{2.3.5}$$

Due to the linearity of Maxwell's equations in the presence of dielectric media, the polarizability of the "matrix-embedded particle" is the sum of two contributions, that is $\alpha(\omega) = \alpha_c(\omega) + \alpha_e(\omega)$, corresponding, respectively, to the two "time-varying free charge sources" involved in the electromagnetic problem. The first one, $\alpha_c(\omega)$, is associated with the (implicit) free charge source giving rise to the applied field $\mathbf{E}_0(t)$. $\alpha_c(\omega)$, which results from the surface polarization charge densities on the dielectric interfaces that are *directly* induced by $\mathbf{E}_0(t)$, is nothing else but the dynamic polarizability of the classical problem (quasistatic limit) in the absence of the conduction electron gas. Its expression is straightforwardly obtained in solving the Poisson equation taking into account the boundary equations at both dielectric interfaces R_i (continuity of the electrostatic potential and of the normal component of the electric displacement) and at large distance ($\mathbf{E}(\mathbf{r},t) \to \mathbf{E}_0(t)$ for $r \to \infty$). The (rather involved) $\alpha_c(\omega)$-expression depends on the input model parameters $\{R_1, R_2, \varepsilon_{ib}(\omega), \varepsilon_m(\omega)\}$. To this classical problem corresponds the electrostatic potential $\phi_c(\mathbf{r},\omega)$ (different expressions result for each nested concentric dielectric medium).

The second contribution, $\alpha_e(\omega)$, is associated with the induced time-varying free charge density $\delta\rho(\mathbf{r},\omega)$. The corresponding dipolar field is sustained by both $\delta\rho(\mathbf{r},\omega)$ and the directly $\delta\rho$-induced polarization charges inside the backgrounds and at the dielectric interfaces. In the presence of dielectric media, the potential energy associated with the classical electromagnetic problem [i.e. $V_{ext}(\mathbf{r},\omega) = -q\phi_c(\mathbf{r},\omega)$] plays the role of the effective external potential energy for the electron gas [S14, S15]. $V_{ext}(\mathbf{r},\omega)$ has therefore to be substituted for the applied external potential energy $V_{ext}^{bare}(\mathbf{r},\omega) = qzE_0$ in the standard TDLDA equations (established in the absence of underlying background dielectric media), which relate the induced electron density $\delta\rho(\mathbf{r},\omega)$ and the polarizability $\alpha_e(\omega)$ to the external potential. One has therefore

$$\delta\rho(\mathbf{r},\omega) = \int \chi(\mathbf{r},\mathbf{r}',\omega)V_{ext}(\mathbf{r}',\omega)d\mathbf{r}' \tag{2.3.6}$$

and

$$\alpha_e(\omega) = -\frac{1}{E_0^2}\int \delta\rho(\mathbf{r},\omega)V_{ext}(\mathbf{r},\omega)d\mathbf{r} = -\frac{1}{E_0^2}\iint \chi(\mathbf{r},\mathbf{r}',\omega)V_{ext}(\mathbf{r},\omega)V_{ext}(\mathbf{r}',\omega)d\mathbf{r}d\mathbf{r}'\,, \tag{2.3.7}$$

where $\chi(\mathbf{r},\mathbf{r}',\omega)$ is the non-local many-body correlation function. Note that the spatial non-locality is an intrinsic feature of the TDLDA formalism since the electron density change at **r** depends on the perturbation applied at any other point **r'** of the system. Within TDLDA, it is assumed that the response of the interacting electronic system can be calculated as in the independent-particle case on condition that the induced variation of the ground-state KS potential energy $V_{eff}(\rho_{gs},\mathbf{r})$, that is

$$\delta V_{eff}(\mathbf{r},\omega) = \int [\frac{\partial V_{eff}(\rho,\mathbf{r}')}{\partial \rho(\mathbf{r}')}]_{\rho_{gs}} \delta\rho(\mathbf{r}',\omega) \tag{2.3.8}$$

$$\delta V_{eff}(\mathbf{r},\omega) = \frac{q^2}{4\pi\varepsilon_0}\int V_c(\mathbf{r},\mathbf{r}')\delta\rho(\mathbf{r}') + \left.\frac{\partial V_{xc}(\rho(\mathbf{r}))}{\partial\rho}\right|_{gs} \delta\rho(\mathbf{r}), \tag{2.3.9}$$

is added to the external one $V_{ext}(\mathbf{r},\omega)$ in eq (2.3.6). The induced electron density $\delta\rho(\mathbf{r},\omega)$ is thus the solution of an implicit equation, from which is derived the integral equation relating $\chi(\mathbf{r},\mathbf{r}',\omega)$ to the independent-electron correlation function $\chi^0(\mathbf{r},\mathbf{r}',\omega)$, namely

$$\chi(\mathbf{r},\mathbf{r}',\omega) = \chi^0(\mathbf{r},\mathbf{r}',\omega) + \iint \chi^0(\mathbf{r},\mathbf{r}_1,\omega)K(\mathbf{r}_1,\mathbf{r}_2,\omega)\chi(\mathbf{r}_2,\mathbf{r}',\omega)d\mathbf{r}_1 d\mathbf{r}_2 \tag{2.3.10}$$

where the kernel $K(\mathbf{r}_1,\mathbf{r}_2,\omega)$ writes as

$$K(\mathbf{r}_1,\mathbf{r}_2) = \frac{q^2}{4\pi\varepsilon_0}V_c(\mathbf{r}_1,\mathbf{r}_2) + \left.\frac{\partial V_{xc}[\rho(r)]}{\partial\rho(r)}\right|_{gs} \delta(\mathbf{r}_1-\mathbf{r}_2). \tag{2.3.11}$$

Finally, $\chi^0(\mathbf{r},\mathbf{r}',\omega)$ can be expressed in terms of the occupied KS orbitals and of the retarded single-particle Green's functions $G(\mathbf{r},\mathbf{r}',\omega)$ of the ground-state KS-Hamiltonian, namely

$$\chi^0(\mathbf{r},\mathbf{r}',\omega) = \sum_i [\varphi_i^*(\mathbf{r})\varphi_i(\mathbf{r}')G(\mathbf{r},\mathbf{r}',\varepsilon_i+\hbar\omega) + \varphi_i(\mathbf{r})\varphi_i^*(\mathbf{r}')G^*(\mathbf{r},\mathbf{r}',\varepsilon_i-\hbar\omega)] \tag{2.3.12}$$

with

$$G(\mathbf{r},\mathbf{r}',E) = \left\langle \mathbf{r}\left|\left[E+i\hbar\delta - H\right]^{-1}\right|\mathbf{r}'\right\rangle, \tag{2.3.13}$$

where *H* is the single-particle KS ground-state Hamiltonian and δ is an infinitesimal positive real parameter. In eq. 2.3.12 the index *i* runs over the occupied ground-state KS-orbitals φ_i of energies ε_i (a temperature of T = 0 K is assumed).

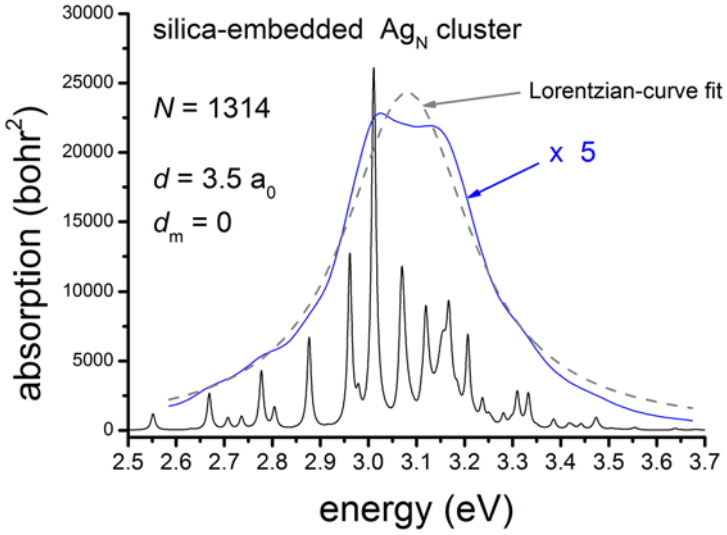

Figure S2.5: Absorption cross-section of silica-embedded Ag_{1314} cluster, for d = 3.5 a_0 and d_m = 0, computed by using two different δ-values in the Green's functions [$\hbar\delta$ = 5 meV (black curve) and $\hbar\delta$ = 60 meV (blue curve, multiplied by a factor of 5 for easier comparison)]. The grey dashed curve is a Lorentzian-shaped curve fit of the blue-curve.

The last relevant free parameter of the model, i.e. δ in eq. (2.3.13), deserves to be discussed. In the TDLDA formalism, the evaluation of the Green's functions requires substituting a finite value for the infinitesimal δ-parameter. Actually δ acts as an *effective* numerical smoothing parameter, which may be used to mimic phenomenologically line broadening arising from physical effects that are disregarded in most models, as for example the dynamical coupling with the vibrations of the ionic lattice, as well as the removal of the $2(2\ell+1)$ KS electron level-degeneracy resulting from the discrete ionic structure, the surface roughness, thermal shape fluctuations or crystal defects (loss of the perfect spherical symmetry). In the present model, this amounts – in a rough picture – to attributing an intrinsic width $2\hbar\delta$ to each bound-bound one-electron excitation line (Lorentzian-shaped curve peak). Therefore, in the absence of Landau damping (see hereafter), the minimum plasmon band width is equal to $2\hbar\delta$. For silver the LSPR band is located below the interband-transitions threshold $\hbar\Omega_{ib}$ and this "asymptotic" value is actually reached for very large sizes.

Throughout this work, free and silica-embedded silver particles, for various d- and d_m-values, have been investigated over the size range [N = 8 ⟶ N = 5000]. It should be emphasized that the modeling could be applied in a broader size range. The maximum size that is selected in the present work is however sufficient to clearly evidence both the red- as well as the blue-shift trends in the size evolution of the LSPR frequency, which, for each parameter set (d, d_m), follow the expected 1/R scaling law. Figure S2.5 displays typical absorption spectra computed from eq. (2.3.5), in using two very different δ-parameters [$\hbar\delta$ = 5 meV (black curve) and $\hbar\delta$ = 60 meV (blue curve)]. In the frame of self-consistent quantum-mechanical models, the decay of the coherent plasmon excitation was attributed for a long time to its coupling, via the particle surface, to one-electron excitations (single particle-hole (*p*-*h*) transitions), a mechanism referred to as the "Landau damping mechanism (LDM)" in cluster physics

[S13, S25]. This mechanism is indeed the main dissipative decay mechanism in the small size range. In a Hamiltonian approach the LDM-induced LSPR broadening can be straightforwardly interpreted in terms of "a discrete state coupled to a continuum" [S29, S30]. The broadening results from the surface-induced coupling of the center-of-mass (CM) coordinate, that is, the dynamical variable corresponding to the collective dipolar excitation, to the intrinsic electronic motions within the CM (the dense *p-h* excitation spectrum, degenerate with the LSPR energy, contributes to this broadening) [S31, S32]. The fragmentation of the LSPR band into *p-h* excitations is clearly evidenced when using a small δ-parameter (black curve in Figure S2.5), but is completely smoothed out when a large δ-value is involved (blue curve). In order to reduce the computational time, the size evolutions determined for each (d, d_m)-parameter set have been extracted from TDLDA spectra computed with $\hbar\delta$ = 60 meV [in the asymptotic large size limit (N > 5000), where the surface effects vanish, the fragmented pattern reduces to a quasi-perfect Lorentzian-shaped curve with a full width at half-maximum close to $2\hbar\delta$ = 120 meV]. It should be mentioned that the asymptotic LSPR bandwidth is not strictly equal $2\hbar\delta$ due to dielectric effects (see eq. 3 in ref. [S31]). Figure S2.6 illustrates the size evolution of the absorption spectra for the parameter set d = 3.5 a_0 and d_m = 6 a_0. Except for the lowermost panel, which corresponds to the largest size investigated in this work (N = 5000), the LSPR band exhibits a size-dependent, asymmetric pattern and shoulders due to the underlying LDM-induced fragmentation. Nevertheless, without the need of consecutive data analysis, a clear blue-shift of the LSPR band with decreasing size is observed for this specific parameter set. In order to avoid a biased analysis that could occur because of the size-dependence of the LSPR band asymmetry, the locations of the LSPR maxima have been systematically determined through a Lorentzian least-squares fit of the overall LSPR pattern (see Figure S2.5; grey curve) for any size and parameter set. It should be pointed out that for very small sizes (typically N < 100), which show only a very small number of LDM-induced "fragments", a much better estimation would consist in determining the centroid of the fragmented pattern. The reason is that the Lorentzian-curve least-squares fit often privileges too much the largest peak in a sparsely fragmented pattern.

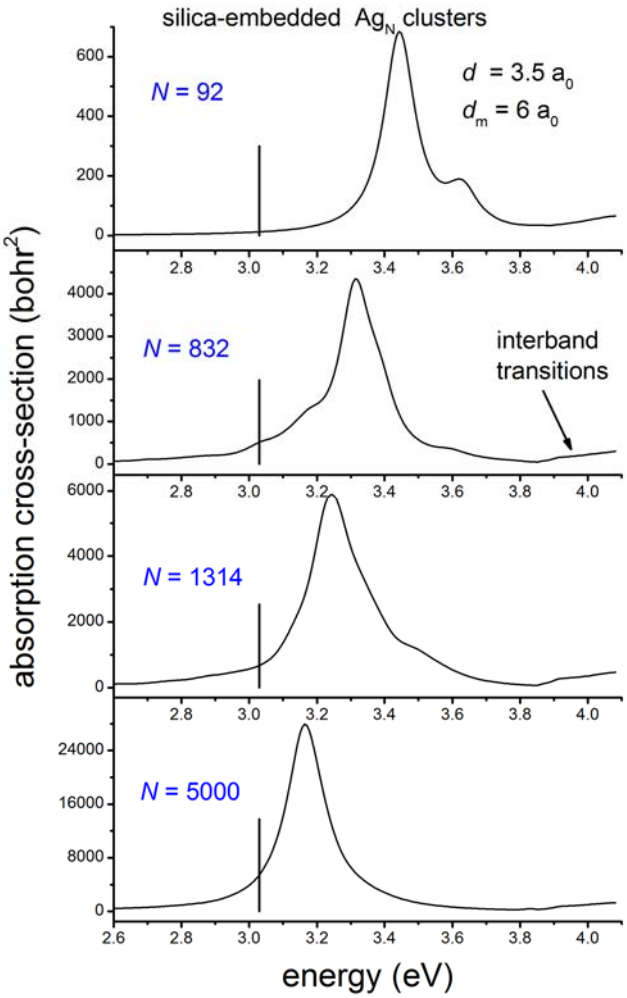

Figure S2.6: Size evolution of the absorption cross-section of silica-embedded Ag_N clusters (N = 92, 832, 1314 and 5000), for d = 3.5 a_0 , d_m = 6 a_0 and $\hbar\delta$ = 60 meV. The short vertical bars, at 3.03 eV, indicate the location of the classical surface plasmon frequency (quasistatic limit).

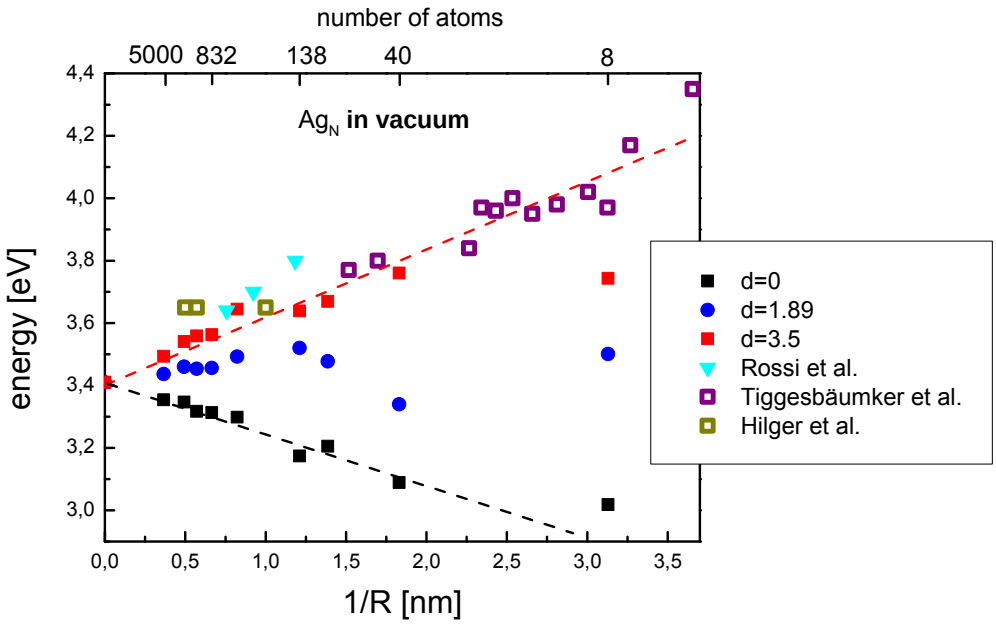

Figure S2.7: Size evolution of the LSPR maxima for free silver clusters. *d* is the thickness of the inner shell of vanishing d-electron polarizability in bohr. The square at 1/*R* = 0 indicates the value of the classical prediction. The light blue triangles are theoretical TD-DFT results [S33], the open squares represent experimental values taken from [S20] and [S34], respectively.

Figure S2.7 shows the results for free Ag_N clusters, for *d* = 0 (black squares), *d* = 3.5 a_0 (red squares) and *d* = 1.89 a_0 (1 Å) (blue circles) for an extended size range with respect to [S10]. For each *d* value, the size-evolution of the LSPR maximum follows an average 1/*R* scaling law. Actually, all finite size- and surface-induced effects, either of quantum or of classical nature, are expected to follow such a generic scaling law, which reflects the surface to volume ratio [S35, S36]. The relative size-dependent differences of most physical/optical quantities, relative to their bulk counterparts (values obtained in the asymptotic large radius limit), scale as $\Delta N_e/N_e$, where N_e is the number of conduction electrons and ΔN_e the "number of electrons" probing the surface region. The extent of spill-out at the surface or the thickness of the layer with reduced ion core polarizability do not depend on the particle size, their relative impact thus varies as 1/R. The three sets of data clearly converge towards the classical asymptotic value 3.41 eV $(1/R \to 0)$. This value is the classical LSPR energy (quasistatic limit) obtained in using the silver dielectric function $\varepsilon_{Ag}(\omega) = \varepsilon_{ib}(\omega) + \varepsilon_D(\omega) - 1$, with the Drude parameters r_s = 3.02 a_0, $m = m_e$ and $\hbar\gamma = 120\ meV$. The convergence towards this asymptotic value proves the accuracy of our TDLDA calculations. For small sizes the large scatter of the results on both sides of the mean 1/*R* scaling law is due to the small number of electrons in the system. Few transitions are then dispersed over a comparably large spectral area and our procedure for determining the LSPR maximum, as pointed out above, leads to relative variations. Note that in the smallest size regime (<100 atoms) the charge of the particle has to be considered as it can lead to systematic blue shifts of the LSPR [S10]. Here, however, we limit our discussion to neutral particles.

For d = 0 a red-shift trend with decreasing size is obtained, whereas a very slight and a noticeable blue-shift trend are obtained for d = 1.89 a_0 and d = 3.5 a_0, respectively. The conspicuous red-shift trend, observed when no shell of vanishing d-electron polarizability is included in the model, strongly challenges the reliability of recent hydrodynamic approaches, developed to introduce the non-locality in the optical response of metal particles [S37-S40]. In fact, these non-self-consistent, simplistic models always predict a blue-shift with decreasing size, the positive 1/R finite-size correction being proportional to the hydrodynamic velocity (~ Fermi velocity) of plasma pressure waves in the metal. In fact, if applied to alkali clusters, a blue-shift trend would also be predicted, in strong disagreement with the numerous pioneering experiments and self-consistent calculations which evidence a red-shift trend instead [S35, S36, S41, S42]. As stated above, the net size trends result from the competition between several factors inducing opposite trends. The present computations, as well as those reported in our previous works [S10, S12], which all involve more realistic ground-state electron densities, show that non-locality by itself is unable to compensate the red-shift trend induced by the spilling out of the conduction electron gas beyond the ionic background radius. For free noble metal clusters the skin of vanishing d-electron polarizability [S16-S19] is responsible for the blue-shift trend observed in absorption spectra as well as in EELS experiments [S20, S28, S37]. As emphasized by Haberland [S43], it is astonishing that nearly three decades of research in cluster science were overlooked in recently published works. To the best of our knowledge, only the improved hydrodynamic model developed by Toscano et al. [S26] gathers all the factors that are relevant for dealing with free silver clusters within the quasi-static approximation, namely: (1) the non-locality which is included through a non-local kinetic energy functional (the Thomas-Fermi-von-Weizsäcker functional is used by these authors), (2) the electron spill-out and (3) the skin of vanishing d-electron polarizability (the value d = 1.89 a_0 was used). Unfortunately, only the size evolution of LSPR frequencies for silver nanowires, which exhibits a slight blue-shift trend, is provided in their paper, preventing their model predictions for spheres to be compared to ours (blue circles in Figure S2.7).

Figure S2.8 displays the results for silica-embedded Ag_N clusters, for d = 3.5 a_0, for various thicknesses of the outer vacuum shell (the color code is indicated in the Figure). The results for the parameter set $d = d_m = 0$ are also shown (black squares). For each parameter set (d, d_m), the size-evolution of the LSPR maximum follows an average 1/R scaling converging towards the classical asymptotic value 3.03 eV $(1/R \to 0)$. This Figure allows providing reasonable semi-quantitative explanations of our experimental findings, in particular those regarding the size trend and time-evolution of the LSPR maxima in the single-particle EELS spectra.

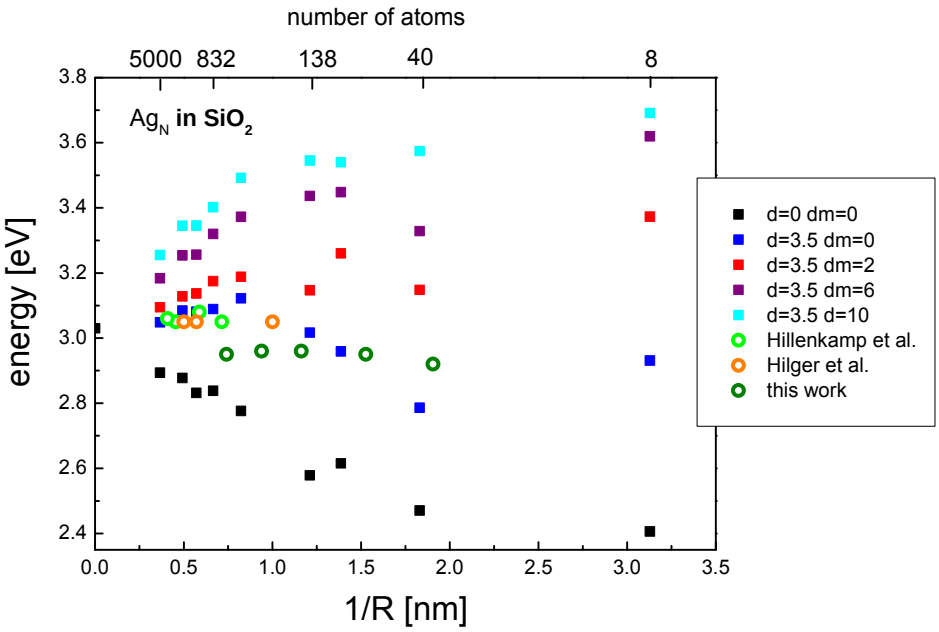

Figure S2.8: Size evolution of the LSPR maxima for silica-embedded silver clusters. *d* (in bohr) is the thickness of the inner shell of vanishing d-electron polarizability. d_m (in bohr) is the thickness of the outer surface shell of vanishing matrix polarizability, simulating the local porosity. The black square at $1/R = 0$ indicates the value for the classical prediction. The open circles represent experimental values taken from [S44] and [S45], respectively.

As stated in the experimental section, the optical absorption spectrum is stable over at least hours, proving that the thickness of the composite Ag_N/silica samples for optics is sufficiently large for ensuring an efficient protection of most particles against oxidation. Keeping in mind that the *d*-value is a phenomenological parameter, Figure S2.8 suggests nevertheless that the local porosity at the particle surfaces in these films is very small. The fact that we obtain reasonable quantitative agreement with the same value for *d* but without the previously necessary phenomenological parameter d_m for the local porosity [S10] strongly supports our model description. One can note that the measured experimental LSPR frequency, 2.95 eV, is slightly lower than the model prediction 3.03 eV. A tiny underestimation of the effective mass (see the Figure 7 in ref. [S23]), as well as that of the $T = 300$ K Wigner-Seitz radius r_s, could explain this slight discrepancy.

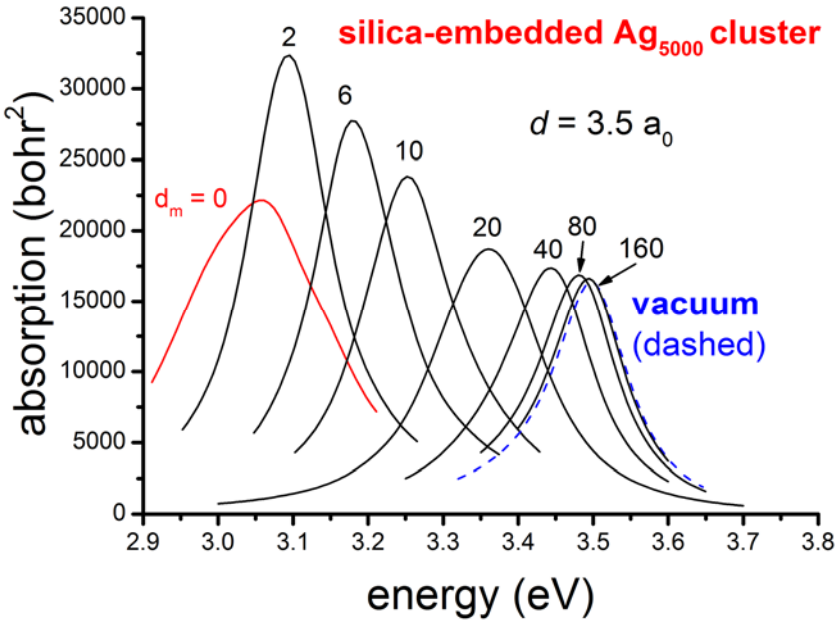

Figure S2.9: Evolution of the absorption spectrum of silica-embedded Ag_{5000} clusters for increasing value of the thickness d_m (in bohr, noted in the figure) of the vacuum-shell simulating the local matrix porosity. The thickness of the inner shell of vanishing d-electron polarizability is d = 3.5 a_0. The blue dashed spectrum corresponds to free Ag_{5000} clusters.

In the case of thin samples, surface oxidation of the silver particles prevents the LSPR band to be observed at the beginning of the electron irradiation, especially for smaller sizes. Under irradiation, the subsequent and progressive removal of light atoms around the particles steadily increases the porosity of the silica shell. This results in a concomitant blue-shift of the LSPR frequency, all the larger the smaller is the particle size, as illustrated in Figure S2.8. In order to estimate the vacuum shell thickness that is required in our modelling for ensuring a blue-shift consistent with the EELS experiments, calculations over an extended d_m-range have been carried out for the largest investigated size N = 5000 (R ≈ 2.73 nm). The results, plotted in Figures S2.9 and 6b of the main text, show the initially very fast and then slower convergence of the absorption spectrum and LSPR maximum towards that of a free Ag_{5000} cluster (the leftmost red square in Figure S2.7). A thickness of about 10 a_0 (≈ 0.5 nm) is found to be sufficient to reproduce a blue-shift comparable to those observed in the STEM-EELS experiments. This small effective value is indeed quite reasonable when compared to the oxide layer thicknesses estimated to ~1 nm.

Finally, we want to comment on the limits of applicability of our model. The most stringent approximation used is the description of the ionic background by a spherical homogeneous polarizable medium (jellium), thereby neglecting all atomic structure. While this assumption certainly reflects the reality for our largest particles very well, it has been shown that below a size of ~100 atoms the atomic structure becomes more and more important [S46-S49]. State-of-the-art calculations demonstrate that different structures lead to different optical responses [S50]. Therefore, the importance of atomistic structure needs to be carefully evaluated. We show in the following that an atomistic description is not necessary for the conclusions we draw in this work.

Three size regimes can –very roughly– be distinguished:

In large particles of several hundred (or more) of atoms, the atomic structure does not play a significant role. Here the particle size is bigger than the Fermi wavelength of the electrons and the particle surface can be considered simply a supplementary scatterer. Effects from crystalline structure or facets are effectively washed out by the wave character of the electrons. Quantum corrections from spill-out or reduced ion-core polarizability, if at all relevant, scale with the surface to volume ratio and result in a general 1/R dependency. An effective modelling using a jellium description for the ionic background is adequate.

Very small clusters, by contrast, must rather be considered molecule-like and the exact atomic structure and the charge state can have significant effects [S48, S50]. Multiply fragmented optical spectra and strong, non-monotonous variations of physical and chemical properties are observed. Many of the very small clusters have low-symmetry ground state structures. The correct description thus requires an extended structural optimization. *Ab-initio* methods are needed for a proper description, but the influence of different corrections and extensions to the functionals used is still highly debated [S47]. Therefore, it is not ensured that the computed optical response strictly reflects the experimental absorption cross-section, which corresponds, in most ensemble experiments, to the net response averaged over a huge number of isomers or thermally-induced distorted geometries and shapes. Our jellium description is clearly very approximate for this size range and we only show the obtained values for the LSPR to demonstrate the general tendency.

In the intermediate size range, ranging from several tens to thousands of atoms, the response in the fragmented optical spectra concentrates in a more and more narrow spectral range with increasing size, and eventually forms the well-known LSPR. The transition from molecular to bulk-like behaviour is not well defined but gradual and remains a topic of intense research. For this intermediate size range the conceptual definition of a plasmon is (still) highly debated in the recent literature [S51-S53].

It is today possible to use ab-initio methods like TDDFT to calculate optical spectra for clusters with several hundred [S33, S54, S55] and up to >1000 atoms [S56], but most of these calculations have only been performed for high-symmetry structures, such as perfect icosahedra, and are extremely costly in computation time. Simple relaxation of a given geometry (as opposed to a full structure optimization) is possible. The results in the literature, however, differ considerably in the absolute values obtained for the same sizes, e.g. in references [S33, S54], probably due to differences in the functionals used.

It should furthermore be noted that all the first principles calculations cited here treat gas phase clusters and that the inclusion of an embedding medium, other than through an effective dielectric shift, is very complicated and time-consuming [S57].

Some direct comparison between jellium and atomistic TDDFT in this intermediate size range is available. For instance, in [S55] atomistic calculations of the optical response of two approximately spherical sodium clusters of similar sizes have been compared with a jellium calculation for the corresponding system (icosahedral Na_{297} vs. fcc-based Na_{331}) and differences of the order of only 0.1 eV are obtained. A similarly small difference has been found for atomistic calculations of silver clusters, where the LSPR of icosahedral Ag_{147} is about 0.1eV higher than that of an fcc-based Ag_{146} [S50]. Only when at least one of the relevant dimensions is reduced to the nanometer scale or below do crystalline structure effects become relevant. This concerns e.g. the near field coupling of large nanoparticle dimers, i.e. across sub-nanometer distances, as used in nanoantennas for field-enhanced spectroscopy [S55]. In our work, only the far field response is discussed.

Two recent publications based on *ab-inito* approaches both report, despite the quantitative differences, a 1/R dependence for the mean LSPR position [S33, S54]. This shows that even in more elaborate calculations the LSPR evolution in the size range of >100 atoms is dominated by the surface/volume ratio. Although we can expect different absolute 1/R dependencies e.g. for series of icosahedra, cuboctahedra or decahedra, as well as a larger spread of individual LSPR energies about the mean value for decreasing size, the overall trend will be the same. In our experiments many isomers, of high and low symmetry, are sampled: in the optical experiments over the particle ensemble, in STEM-EELS over time. We consequently average over all these structures, whose presence mainly results in a broadening of the resonance.

In conclusion, we show that, at least for the size range between roughly 1-10 nm in diameter, the size variations of the mean LSPR are dominated by electronic effects such as spill-out and the influence of d electrons rather than by the crystalline structure of the silver nanoparticles. Structureless jellium-type model approaches [S13] are quite appropriate and reasonable for investigating mean size trends over large size ranges, as well as for the comparison between various metallic species. Moreover, only such an approximate ionic background description allows us to carry out fast calculations over a very large size range (up to 5000 silver atoms in the present work) for many model parameter sets (e.g. embedding matrix and layer thicknesses of reduced refractive index). It should be mentioned that the jellium model, applied extensively at the end of the last century in the cluster physics community, remains of widespread use in the plasmonics community, and was applied for example for handling more complex systems, such as spherical concentric core-shell nanoparticles [S58] or metal dimers [S59, S60].

Another widely used approach to the theoretical description of metal nanoparticles of various sizes, shapes and materials, especially in the plasmonics community, is a hydrodynamic model, as already stated above [S37-S40]. It should be emphasized that this semi-classical model presents several significant advantages, namely its intuitive approach, the inclusion of spatial non-locality at different

levels of sophistication, its comparably easy implementation and lastly its adaptability to more complex geometries, beyond high-symmetry structures like concentric spheres. Care has, however, to be taken, when strong simplifying assumptions are used. In particular, in assuming a hard-walled and stepwise jellium-like ground-state potential with the corresponding electron density forced to zero at the particle surface, the spill-out is clearly neglected. The corresponding simulations cannot correctly reproduce the opposite tendencies for alkaline and noble metal particles, i.e. red and blue shifts of the LSPR with decreasing size. The influence of non-locality on the one hand and reduced ion-core polarizability on the other need to be distinguished with precaution.

S2.4 Simulation of the plasmonic response of oxidized core-shell $Ag/Ag_xO/SiO_2$ nanoparticles

In order to corroborate our interpretation that some of the largest particles investigated by STEM-EELS show initial LSPR energies below the expected value of 3 eV (cf. Fig. 4) because of oxidation, we calculated absorption curves within classical Mie theory for concentric core@shell $Ag@Ag_xO$ nano-spheres embedded in a silica matrix [S61]. The absorption cross-sections have been calculated in the dipolar approximation for various oxidation ratios (OR), defined as the oxide shell to metal core volume ratio $(R'^3-R_c^3)/R'^3$ (R_c designates the Ag-core radius, and R' the total radius). For 0% oxidation, the pure silver radius is R = 5 nm. The calculation of the thickness of the shell for a given level of oxidation by using the lattice parameters of Ag_2O (a=0.472 nm [S62]) is detailed in ref. [S63]. The increased lattice parameter of the silver oxide results in an increasing total diameter R' upon oxidation. The calculations have been performed with the dielectric function for silver (as described above) and those deduced from the work of Qiu et al. [S64] for oxidized silver (see ref. [S63] for further details). The matrix dielectric function used here is extracted from the tabulated bulk-silica data [S21].

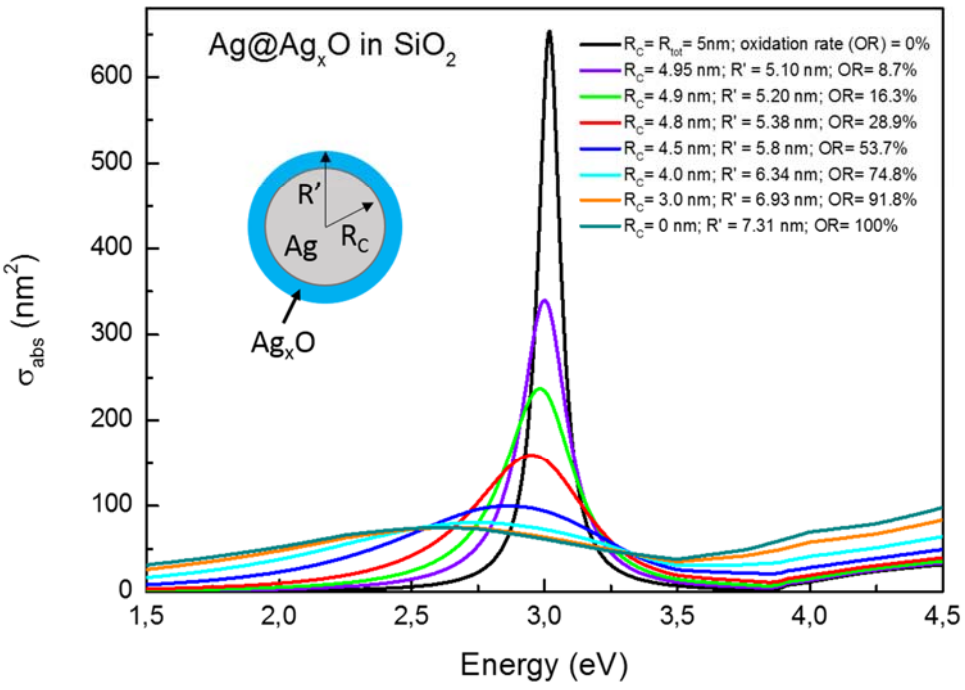

Figure S2.10: Calculated absorption cross-sections within the dipolar approximation in a silica-embedded core/shell $Ag@Ag_xO$ spherical geometry for increasing oxidation rates (OR).

The spectral position of the resonance is at 3.03 eV for non-oxidized NPs, as discussed in section S2.3, and shifts to <2.7 eV for high oxidation rates. These classical calculations do not depend on the size of the nanoparticles. Only the amplitude of the absorption cross section changes but the oxidation-dependent shift is the same for all the large particles studied. A degree of oxidation of ~75% thus leads to a shift of the LSPR of the core/shell particle to ~2.75 eV, where the most red-shifted signals were detected. The decreasing width of the peak upon progressing reduction is consistent with our EELS

data (cf. Figs. 3 and S1.9) and with the literature. In reference [S2], figure 3 demonstrates the red shift accompanied by an increasing width as a function of increasing refractive index of the surrounding matrix.

Supplementary references

[S1] Koga, K. and Sugawara, K. *Surf. Sci.* **529**(1), 23 – 35 (2003).

[S2] Kreibig, U., Gartz, M., Hilger, A., and Neuendorf, R. *Nanostruc. Mater.* **11**, 1335–42 (1999).

[S3] García de Abajo, F. J. and Howie, A. *Phys. Rev. B* **65**, 115418 (2002).

[S4] Garcá de Abajo, F. J. *Rev. Mod. Phys.* **82**, 209–275 (2010).

[S5] García de Abajo, F. J. and Kociak, M. *Phys. Rev. Lett.* **100**, 106804 (2008).

[S6] Ferrell, T. L., Warmack, R. J., Anderson, V. E., and Echenique, P. M. *Phys. Rev. B* **35**, 7365–7371 (1987).

[S7] Wang, Z. *Micron* **27**(3), 265 – 299 (1996).

[S8] Rakic, A. D., Djurišic, A. B., Elazar, J. M., and Majewski, M. L. *Appl. Opt.* **37**(22), 5271–5283 (1998).

[S9] Henrard, L. and Lambin, P. *J. Phys. B: At., Mol. Opt. Phys.* **29**(21), 5127 (1996).

[S10] Lermé, J., Palpant, B., Prével, B., Pellarin, M., Treilleux, M., Vialle, J. L., Perez, A., and Broyer, M. *Phys. Rev. Lett.* **80**(23), 5105 (1998).

[S11] Lermé, J., Palpant, B., Prével, B., Cottancin, E., Pellarin, M., Treilleux, M., Vialle, J. L., Perez, A., and Broyer, M. *Eur. Phys. J. D* **4**(1), 95–108 (1998).

[S12] Cottancin, E., Celep, G., Lermé, J., Pellarin, M., Huntzinger, J. R., Vialle, J. L., and Broyer, M. *Theor. Chem. Acc.* **116**, 514 (2006).

[S13] Ekardt, W. *Phys. Rev. B* **31**, 6360–6370 (1985).

[S14] Lermé, J., Palpant, B., Cottancin, E., Pellarin, M., Prével, B., Vialle, J. L., and Broyer, M. *Phys. Rev. B* **60**, 16151–16156 (1999).

[S15] Lermé, J. *Eur. Phys. J. D* **10**(2), 265–277 (2000).

[S16] Liebsch, A. *Phys. Rev. B* **48**, 11317–11328 Oct (1993).

[S17] Fedrigo, S., Harbich, W., and Buttet, J. *Phys. Rev. B* **47**, 10706 (1993).

[S18] Kresin, V. V. *Phys. Rev. B* **51**, 1844–1849 (1995).

[S19] Serra, L. and Rubio, A. *Z. Phys. D* **40**(1), 262–264 Mar (1997).

[S20] Tiggesbäumker, J., Köller, L., Meiwes-Broer, K.-H., and Liebsch, A. *Phys. Rev. A* **48**, R17492 (1993).

[S21] Palik, E. *Handbook of Optical Constants of Solids*. Academic, New York, (1985).

[S22] Kittel, C. *Introduction to Solid State Physics*. Wiley, 7th edition edition, (1995).

[S23] Ehrenreich, H. and Philipp, H. R. *Phys. Rev.* **128**, 1622–1629 (1962).

[S24] Gunnarsson, O. and Lundqvist, B. I. *Phys. Rev. B* **13**, 4274–4298 (1976).

[S25] Yannouleas, C. and Broglia, R. A. *Phys. Rev. A* **44**, 5793–5802 (1991).

[S26] Toscano, G., Straubel, J., Kwiatkowski, A., Rockstuhl, C., Evers, F., Xu, H., Asger Mortensen, N., and Wubs, M. *Nat. Commun.* **6**, 7132 (2015).

[S27] Keller, O., Xiao, M., and Bozhevolnyi, S. *Opt. Commun.* **102**(3), 238 – 244 (1993).

[S28] Scholl, J. A., Koh, A. L., and Dionne, J. A. *Nature* **483**, 421 (2012).

[S29] Cohen-Tannoudji, C., Diu, B., and Laloe, F. *Quantum Mechanics*. Wiley, (1991).

[S30] Fano, U. *Phys. Rev.* **124**, 1866–1878 (1961).

[S31] Lermé, J. *J. Phys. Chem. C* **115**(29), 14098–14110 (2011).

[S32] Lermé, J., Bonnet, C., Lebeault, M.-A., Pellarin, M., and Cottancin, E. *J. Phys. Chem. C* **121**(10), 5693–5708 (2017).

[S33] Rossi, T. P., Kuisma, M., Puska, M. J., Nieminen, R. M., and Erhart, P. *J. Chem. Theory Comput.* **13**(10), 4779–4790 (2017).

[S34] Hilger, A., Tenfelde, M., and Kreibig, U. *Appl. Phys. B* **73**, 361–372 (2001).

[S35] de Heer, W. A. *Rev. Mod. Phys.* **65**, 611 (1993).

[S36] Brack, M. *Rev. Mod. Phys.* **65**, 677 (1993).

[S37] Raza, S., Stenger, N., Kadkhodazadeh, S., Fischer, S. V., Kostesha, N., Jauho, A.-P., Burrows, A., Wubs, M., and Mortensen, N. A. *Nanophotonics* **2**, 131–138 (2013).

[S38] Mortensen, N. A., Raza, S., Wubs, M. Søndergaard, T., and Bozhevolnyi, S. I. *Nat. Commun.* **5**, 3809 (2014).

[S39] Christensen, T., Yan, W., Raza, S., Jauho, A.-P., Mortensen, N. A., and Wubs, M. *ACS Nano* **8**(2), 1745–1758 (2014).

[S40] Raza, S., Yan, W., Stenger, N., Wubs, M., and Mortensen, N. A. *Opt. Express* **21**(22), 27344–27355 (2013).

[S41] Kresin, V. V. *Phys. Rep.* **220**, 1 (1992).

[S42] Bréchignac, C., Cahuzac, P., Leygnier, J., and Sarfati, A. *Phys. Rev. Lett.* **70**, 2036–2039 (1993).

[S43] Haberland, H. *Nature* **494**, E1 (2013).

[S44] Hillenkamp, M., Di Domenicantonio, G., Eugster, O., and Félix, C. *Nanotechnology* **18**, 015702 (2007).

[S45] Hilger, A., Cüppers, N., Tenfelde, M., and Kreibig, U. *Eur. Phys. J. D* **10**, 115–118 (2000).

[S46] Bonacic-Koutecky, V., Fantucci, P., and Koutecky, J. *Chem. Rev.* **91**(5), 1035–1108 (1991).

[S47] Anak, B., Bencharif, M., and Rabilloud, F. *RSC Adv.* **4**, 13001–13011 (2014).

[S48] Rabilloud, F. *J. Chem. Phys.* **141**(14), 144302 (2014).

[S49] Weissker, H.-C. and Lopez-Lozano, X. *Phys. Chem. Chem. Phys.* **17**, 28379–28386 (2015).

[S50] Weissker, H.-C. and Mottet, C. *Phys. Rev. B* **84**, 165443 (2011).

[S51] Bernadotte, S., Evers, F., and Jacob, C. R. *J. Phys. Chem. C* **117**(4), 1863–1878 (2013).

[S52] Bursi, L., Calzolari, A., Corni, S., and Molinari, E. *ACS Photonics* **3**(4), 520–525 (2016).

[S53] Zhang, R., Bursi, L., Cox, J. D., Cui, Y., Krauter, C. M., Alabastri, A., Manjavacas, A., Calzolari, A., Corni, S., Molinari, E., Carter, E. A., García de Abajo, F. J., Zhang, H., and Nordlander, P. *ACS Nano* **11**(7), 7321–7335 (2017).

[S54] Baseggio, O., De Vetta, M., Fronzoni, G., Stener, M., Sementa, L., Fortunelli, A., and Calzolari, A. *J. Phys. Chem. C* **120**(23), 12773–12782 (2016).

[S55] Zhang, P., Feist, J., Rubio, A., Garcá-González, P., and Garcá-Vidal, F. J. *Phys. Rev. B* **90**, 161407 (2014).

[S56] Iida, K., Noda, M., Ishimura, K., and Nobusada, K. *J. Phys. Chem. A* **118**(47), 11317–11322 (2014).

[S57] Yu, C., Harbich, W., Sementa, L., Ghiringhelli, L., Aprá, E., Stener, M., Fortunelli, A., and Brune, H. *J. Chem. Phys.* **147**(7), 074301 (2017).

[S58] Kulkarni, V., Prodan, E., and Nordlander, P. *Nano Lett.* **13**(12), 5873–5879 (2013).

[S59] Zuloaga, J., Prodan, E., and Nordlander, P. *Nano Lett.* **9**(2), 887–891 (2009).

[S60] Marinica, D., Kazansky, A., Nordlander, P., Aizpurua, J., and Borisov, A. G. *Nano Letters* **12**(3), 1333–1339 (2012).

[S61] Cottancin, E., Broyer, M., Lermé, J., and Pellarin, M. *Handbook of Nanophysics: Nanoelectronics and Nanophotonics*, chapter Optical Properties of Metal Clusters and Nanoparticles. CRC Press, Boca Raton, FL, USA (2011).

[S62] Bock, F., Christensen, T., Rivers, S., Doucette, L., and Lad, R. *Thin Solid Films* **468**, 57 – 64 (2004).

[S63] Grillet, N., Manchon, D., Cottancin, E., Bertorelle, F., Bonnet, C., Broyer, M., Lermé, J., and Pellarin, M. *J. Phys. Chem. C* **117**, 2274–2282 (2013).

[S64] Qiu, J.-H., Zhou, P., Gao, X.-Y., Yu, J.-N., Wang, S.-Y., Li, J., Zheng, Y.-X., Yang, Y.-M., Song, Q.-H., and Chen, L.-Y. *J. Korean Phys. Soc.* **46**, 269 (2005).